Reactivity at the electrode-electrolyte interfaces in Li-ion and gel electrolyte lithium batteries for LiNi0.6Mn0.2Co0.2O2 with different particle sizes

Adrien Soloy, Delphine Flahaut, Dominique Foix, Joachim Allouche, Germain Vallverdu, Erwan Dumont, Lucille Gal, François Weill, Laurence Croguennec

▶ To cite this version:

Adrien Soloy, Delphine Flahaut, Dominique Foix, Joachim Allouche, Germain Vallverdu, et al.. Reactivity at the electrode-electrolyte interfaces in Li-ion and gel electrolyte lithium batteries for LiNi0.6Mn0.2Co0.2O2 with different particle sizes. ACS Applied Materials & Interfaces, 2022, 5 (5), pp.5617-5632. 10.1021/acsami.2c04249 . hal-03684124

Reactivity at the electrode-electrolyte interfaces in Li-ion and gel electrolyte lithium batteries for $LiNi_{0.6}Mn_{0.2}Co_{0.2}O_2$ with different particle sizes

Adrien Soloy[1], *Delphine Flahaut*[2,4,*], *Dominique Foix*[2,4], *Joachim Allouche*[2,4], *Germain Salvato Vallverdu*[2,4], *Erwan Dumont*[3], *Lucille Gal*[3], *François Weill*[1,4,5] *and Laurence Croguennec*[1,4,5,*]

[1] Univ. Bordeaux, CNRS, Bordeaux INP, ICMCB UMR 5026, F-33600 Pessac, France

[2] Université de Pau et des Pays de l'Adour, E2S UPPA, CNRS, IPREM UMR 5254, 64000 Pau,
France

[3] SAFT, Direction de la Recherche, 33074 Bordeaux, France

[4] RS2E, Réseau Français sur le Stockage Electrochimique de l'Energie, FR CNRS 3459,
F-80039 Amiens Cedex 1, France

[5] ALISTORE-ERI European Research Institute, FR CNRS 3104, F-80039 Amiens Cedex 1,
France

KEYWORDS: Li-ion battery, All-Solid-State batteries, Layered oxide, NMC, Gelified electrolyte Morphology, Reactivity

ABSTRACT

The layered oxide $LiNi_{0.6}Mn_{0.2}Co_{0.2}O_2$ is a very attractive positive electrode material, as shown by good reversible capacity, chemical stability and cyclability upon long range cycling in Li-ion batteries and, hopefully, in a near future, in all-solid-state batteries. Three samples with variable primary particle sizes of 240 nm, 810 nm and 2.1 µm in average and very similar structures close to the ideal 2D layered structure (less than 2% Ni^{2+} ions in Li^{+} sites) were obtained by coprecipitation followed by solid-state reaction at high temperature. The electrochemical performances of the materials were evaluated in a conventional organic liquid electrolyte in Li-ion batteries and in a gel electrolyte in all-solid-state batteries. The positive electrode/electrolyte interface was analysed by X-Ray photoelectron spectroscopy in order to determine its composition and the extent of the degradation of the lithium salt and the carbonate solvents after cycling, taking into account the changes in particle size of the positive electrode material and the nature of the electrolyte.

INTRODUCTION

Lithium-ion batteries (LiBs) are already widely used in many applications, especially for electronics, stationary storage and electric vehicles. The rapid development of renewable energies and electric transportation is especially responsible for the exponential demand for LiBs with higher energy densities.[1] Different strategies are followed in order to supply this demand: (i) optimization of high energy density positive electrode materials such as Li-rich or Ni-rich layered oxides or high voltage spinel $LiNi_{1/2}Mn_{3/2}O_4$,[2–4] (ii) migration towards Li metal all-solid-state batteries (ASSBs) with the replacement first of the organic liquid electrolyte by a solid (inorganic, polymer or hybrid) electrolyte and then of the graphite by Li metal at the negative electrode,[5–7] and (iii) development of new battery chemistries such as Li/S or Li-air batteries.[8] One of the main problems for the first strategy remains the safety issues, reinforced when combining organic liquid electrolyte with high voltage positive electrode materials. Indeed, their instability in the charge state of the battery or at high cycling rates can lead to oxygen gas and heat release, to thermal runaway with electrolyte decomposition and flammability, and possibly to fire of the battery.[9–13] One of the main concerns to develop even higher energy LiBs remains thus the optimization of organic electrolytes with appropriate additives to stabilize the electrode-electrolyte interfaces when cycled at high potential and/or at high rate.[14–21] The additional motivation beyond the higher energy density for the development of ASSBs is that, as free of organic solvents, they appeared as another effective way to address the safety issues. However, the performances of those systems remain poor, as facing a series of challenges to be solved before their development and introduction into the market: mainly, interfacial irreversible reactivity[6,22–24] and strong mechanical strains[25–29] leading to poor Li^+ ion diffusion at the solid-

solid electrode-electrolyte interfaces and to formation of cracks, Li dendrites[5,30–32] until possible short-circuits and safety concerns.

The layered oxide $LiNi_{0.6}Mn_{0.2}Co_{0.2}O_2$ (NMC622) is a very attractive positive electrode material as already extensively reported, with its good reversible capacity (up to 180-190 mAh/g), chemical stability and cyclability upon long range cycling in Li-ion batteries.[33–41] Recently we have explored a large panel of synthesis conditions to tailor the primary particle size of NMC622 powders from 170 nm to 2.1 µm.[42] Their electrochemical performance in Li-ion batteries and surface reactivity have been shown to be highly sensitive to cycling conditions (C-rates and potential windows), as well as to primary particle size. Indeed, larger particles have shown the formation of solid electrolyte interphase with a larger proportion of lithium salt degradation products versus solvents degradation products, induced especially by the larger amount of Li_2CO_3 at their pristine surface. Furthermore, degradation of the lithium salt was favoured at higher cycling rate, whereas in a lesser extent that of the organic solvents in larger potential windows with a higher cut-off voltage. In this study, we have focused our interest on three different NMC622 materials with particle sizes of 240 nm, 810 nm and 2.1 µm, to compare their electrochemical performance in conventional LiBs with an organic liquid electrolyte and in Li metal ASSBs with a gel electrolyte. The reactivity was studied in both systems as a function of the primary particle size, combining X-ray diffraction (XRD), X-ray photoelectron spectroscopy (XPS) and scanning electron microscopy (SEM).

EXPERIMENTAL SECTION

The synthesis of the three $Li(Ni_{0.6}Mn_{0.2}Co_{0.2})O_2$ layered oxides studied here is described in details elsewhere.[42] The mixed transition metal (TM) hydroxide is intimately mixed with lithium carbonate Li_2CO_3 (Sigma-Aldrich, ≥99%) such as an excess of 5 wt.% versus the Li/TM ratio of 1.05 is used. Thermal treatments are performed at increasing temperatures to promote the particle growth, i.e. at 810°C, 900°C and 930°C, and under O_2 flow to favour the stabilization of a 2D structure with almost no Ni^{2+} ions in excess in the Li^+ sites. The samples are named in the following according to their synthesis conditions: lithiation temperature (°C) - weight percentage of Li_2CO_3 excess - atmosphere.

As reported in reference 42, the cationic composition of the lithiated layered oxides was determined by Inductively Coupled Plasma - Optical Emission Spectrometry (ICP-OES) (Varian ICP/OES 720 ES), whereas the carbon content of the powders was also determined using a CHNS elemental Thermo Fischer Scientific analyser equipped with an automatic sampler. Powder X-Ray diffraction (XRD) patterns were recorded using a PANalytical X'Pert MPD Pro diffractometer equipped with a Cu radiation X-ray tube, in the angular range of 10-80° (2θ) with 0.008° intervals, and for a total acquisition time of around 35 hrs. The collected XRD patterns were refined by the Rietveld method using FullProf software.[43] The powders, as well as the electrodes and their cross sections before and after cycling, were observed by scanning electron microscopy (JEOL 6700F and TESCAN Vega), after their metallization by gold deposition. The cross-section of the electrodes was performed using a cross section polisher (Gatan Ilion II 697). A wedge-type polishing at 90° was performed at a 5 kV voltage for 2 hrs and at 1 kV for 1h. Granulometry measurements were performed using a Malvern Mastersizer 2000. The powders were previously dispersed in distilled water and sonicated for 1 min. BET surface areas were determined using a Micromeritics 3FLEX analyser. The powders were previously degassed under vacuum at 90°C for 1 hr and then at 150°C for 10 hrs.

The surface composition of the pristine powders, pristine electrodes and corresponding cycled electrodes was determined by XPS using an ESCALAB 250 Xi spectrometer with a monochromatized Al-Kα X-Ray source (hν = 1486.6 eV). A neutraliser gun was used to minimize surface charging. For the pristine powders, the spectral calibration was carried out using the C-C/C-H component (285 eV) originated from the surface carbon contamination in C1s core peaks. For the electrodes, it was carried out using the CF_2 component (291 eV) originated from the PVDF polymeric binder in C1s core peaks. The peak fitting process was carried out using a non-linear Shirley-type background. The peak positions and areas were optimized by weighted least-squares calculation method using 70% Gaussian and 30% Lorentzian line shapes. The quantification of surface composition was based on Scofield's relative sensitivity factors corrected by specific values depending on the apparatus.[44] The quantification and spectra fitting were carried out using CASA XPS software.

The samples were electrochemically tested in CR2032-type coin cells prepared in an argon-filled glovebox and consisting of a positive electrode and a lithium foil as negative electrode, separated by two Celgard 2325 separators. The positive electrodes were prepared by coating a slurry on an aluminium foil as current collector. The slurry was prepared by mixing the active material with Super C65 carbon black and Solef 5130 polyvinylidene fluoride (PVDF) binder (91:5:4 wt.%) in N-methyl-2-pyrrolidone (NMP) (Scharlau, GC head space grade). The samples were cycled versus Li metal, either in a liquid organic electrolyte consisting of $LiPF_6$ (1M) in a mixture of cyclic and linear carbonate solvents, or in a gel electrolyte consisting of $LiPF_6$ in carbonated solvents and liquid in its pristine state. The gelified electrolyte, which composition cannot be disclosed but similar to that described in reference 45, was obtained after its polymerization *in situ* at 60°C overnight after assembling the coin-cell with exactly the same protocol to that already described.[42] The coin cells were cycled using a VMP (Biologic) in galvanostatic mode. After cycling, the electrodes were recovered in an Ar-filled glovebox to prevent any evolution in air atmosphere before their characterization, and they were washed with dimethyl carbonate in large excess in order to remove the salt and dried under vacuum. The protocol was similar whatever the electrolyte, liquid or gelified.

RESULTS AND DISCUSSION

Structural and physico-chemical characterizations

The structure of the three $Li(Ni_{0.6}Mn_{0.2}Co_{0.2})O_2$ layered oxides was analysed by X-ray diffraction. Their X-ray diffraction patterns are compared in **Figure 1**. They reveal that each compound is a pure layered oxide with a sharpening of the diffraction lines, reflecting an increase of the crystallinity of the powder with the increase of the synthesis temperature from 810°C to 900°C, as shown by the increase of the Full Width at Half Maximum (FWHM) of the (003) and (104) peaks as reported in **Table 1**. As already reported in details in reference 42, they crystallize in an α-$NaFeO_2$-type layered structure described in the *R-3m* space group and close to a perfect 2D structure, as determined by Rietveld refinement of their XRD patterns and as shown by the presence of less than 2% of Ni^{2+} in excess in the Li^+ sites. The structural parameters of these three materials are gathered in **Table 1**, with also the description of the cationic distribution between the Li$^+$ sites on one side and the transition metal sites on the other side. This description is based on a global charge compensation and on the stabilization of Ni in the divalent state in the interslab space and of Co and Mn in the trivalent and tetravalent states in the slabs respectively.[46] These three samples are very similar layered oxides from a composition and structural point of view, with similar cell parameters, amount of Ni^{2+} in the Li$^+$ sites and cationic distribution within the layered framework. Ni^{2+}, Ni^{3+}, Co^{3+} and Mn^{4+} cations are in fact randomly distributed in the transition metal sites. This structural study confirms as reported in reference 42 that a thermal treatment under oxygen with a small excess of Li precursor favours the formation of almost ideal 2D layered structures at 810°C, 900°C and 930°C.

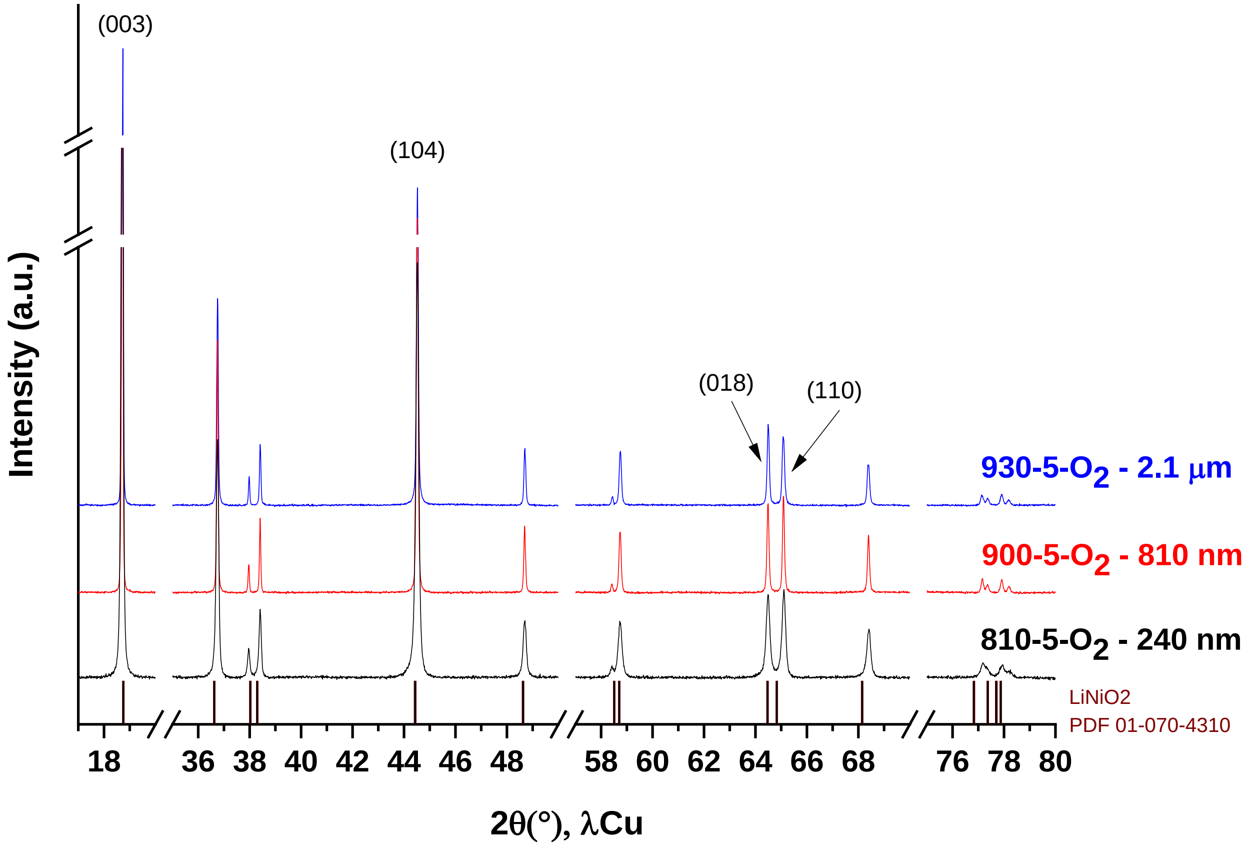

Figure 1. X-Ray diffractions patterns obtained for the synthesized samples. The indexation of the diffraction lines is given in the *R-3m* space group.

Table 1. Lattice parameters, c/a ratios, FWHM of the (003) and (104) peaks, compositions and cationic distributions calculated from the Rietveld refinement of the X-Ray diffraction patterns. Average primary particle sizes determined by measuring 100 primary particles on SEM pictures with the software ImageJ.

Samples	**a(Å)**	**c(Å)**	**c/a**	**FWHM (003)**	**FWHM (104)**	**Composition and cation distribution**	**SEM average primary particle size**
930-5-O_2	2.86356(3)	14.2006(4)	4.9591(2)	0.05	0.08	$(Li^{+}_{0.982(3)}Ni^{2+}_{0.018(3)})(Ni^{2+}_{0.222(4)}Ni^{3+}_{0.371(5)}Mn^{4+}_{0.204(1)}Co^{3+}_{0.204(1)})O_2$	2.1 µm
900-5-O_2	2.86298(3)	14.2021(3)	4.9606(2)	0.05	0.08	$(Li^{+}_{0.985(3)}Ni^{2+}_{0.015(3)})(Ni^{2+}_{0.218(4)}Ni^{3+}_{0.376(5)}Mn^{4+}_{0.203(1)}Co^{3+}_{0.203(1)})O_2$	810 nm
810-5-O_2	2.86252(6)	14.2014(6)	4.9612(3)	0.09	0.14	$(Li^{+}_{0.982(3)}Ni^{2+}_{0.018(3)})(Ni^{2+}_{0.222(4)}Ni^{3+}_{0.371(5)}Mn^{4+}_{0.204(1)}Co^{3+}_{0.204(1)})O_2$	240 nm

The composition of the samples was verified by ICP-OES analyses; the results are shown in **Table S1** in supplementary information. The three samples show compositions in transition metals close to the targeted ones, i.e. the stoichiometry Ni:Mn:Co of 6:2:2. A slight overlithiation is observed with Li/TM ratios larger than 1 for the 3 samples, despite a Li/TM ratio slightly smaller than 1 in the layered structures (0.96-0.97 obtained from XRD refinements). Traces of carbon were estimated by gas chromatography analyses to be smaller than 1 wt.%. Combined with the Li excess, it suggests the presence of Li_2CO_3 in the powders despite not detected by XRD. This carbonate can be, either a residue of the Li precursor used in excess during the synthesis, or formed by reaction of the lithiated layered oxide with ambient air after the synthesis.[47–49]

Figure 2 compares the morphology of the three compounds. As shown in reference 42 that is devoted to the screening of synthesis conditions to control the formation of NMC622 with 2D structure and tailored morphology, the average primary particle size increases with the lithiation temperature from 240 nm at 810°C, to 810 nm at 900°C and to 2.1 µm at 930°C (**Table 1)**. These sizes were estimated by measuring 100 particles on SEM pictures with the software ImageJ. The corresponding particle size distributions are also compared in **Figure 2**, they widen with the increase of the lithiation temperature. To get more insight into the morphology of the three materials, laser granulometry measurements were performed with or without applying 1 min sonication. **Figure S1** gives the distribution in number of the particles and aggregates' sizes. These results obtained by SEM and laser granulometry confirm that smaller primary particles are obtained for the 810-5-O_2 sample and larger primary particles are obtained for the 930-5-O_2 sample. The 810-5-O_2 size distribution expands from 0.1 to 0.5 µm for the primary particles observed by SEM (**Figure 2b**), and from 0.3 to 10 µm for the primary particles and aggregates observed by laser granulometry (**Figure S1a**). The 930-5-O_2 size distribution expands from 0.8 to 4.2 µm for the primary particles observed by SEM (**Figure 2f**), and from 0.8 to 10 µm for the primary particles and aggregates observed by laser granulometry (**Figure S1a**). Despite at the limit of accuracy of the technique, a trend was observed in the variation of the BET specific surface area as a function of the synthesis temperature. As shown in **Table S2**, it decreases from around 3 m^2/g for the 240 nm particles (810-5-O_2 sample) to around 1 m^2/g for the 2.1 µm particles (930-5-O_2 sample), and in parallel the pore volume also decreases from around 0.009 cm^3/g to 0.002 cm^3/g respectively.

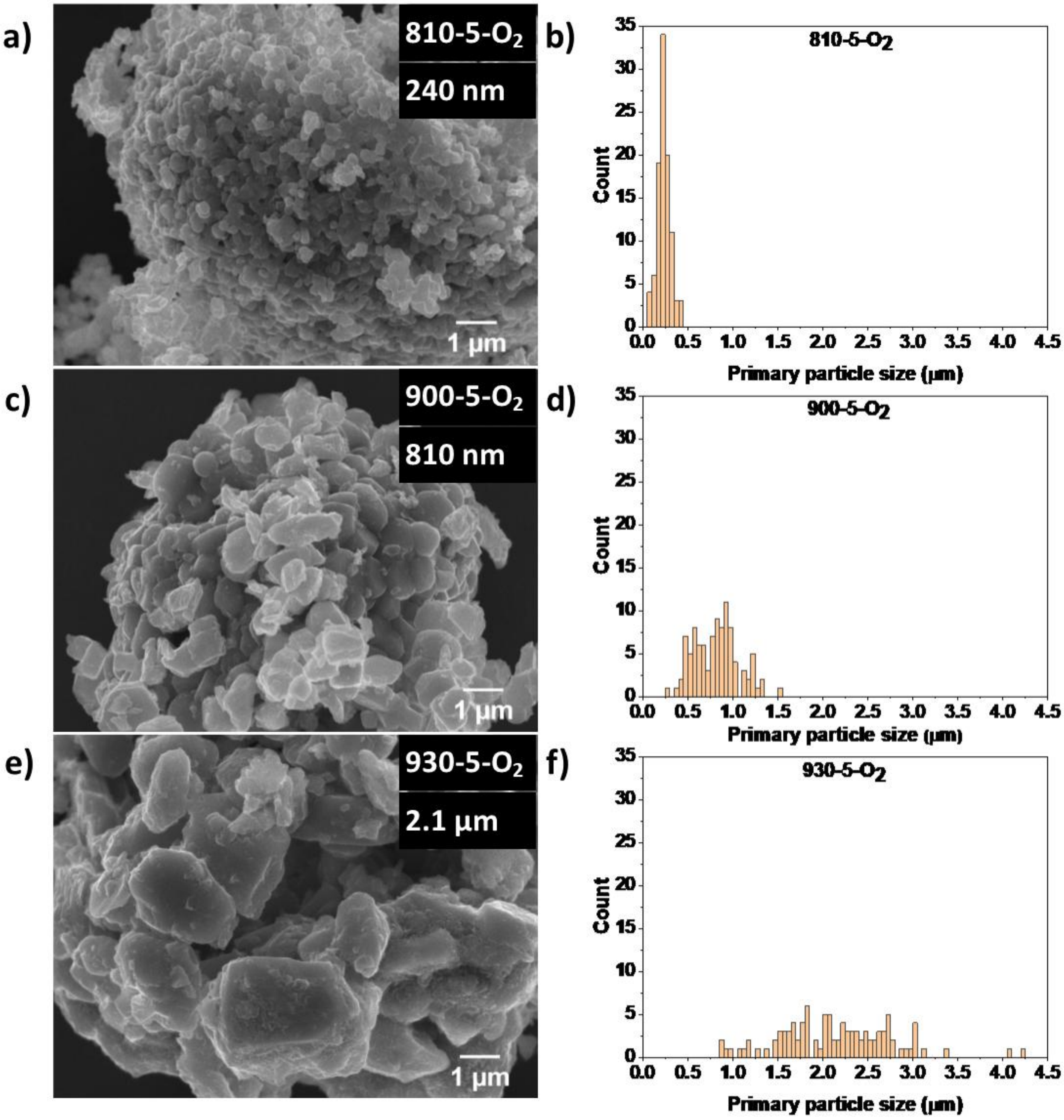

Figure 2. Morphologies obtained for the samples synthesized at 810°C (a), 900°C (c) and 930°C (e). An increase of the average primary particle size from 240 nm to 2.1 µm is observed between 810°C and 930°C. These average sizes were determined by measuring 100 particles using the software ImageJ (b, d and f).

Surface analyses

The surface of these samples was analysed by XPS. **Figure 3** compares the C1s, O1s and Ni3p-Co3p-Li1s-Mn3p spectra collected for the three compounds. Chemisorbed contamination species are detected at the surface of the particles and are responsible for several contributions in the C1s and O1s spectra. The C1s spectra are decomposed into four contributions observed at 285.0, 286.5, 288.7 and 290.0 eV and corresponding to C-C/C-H, C-O, C=O/O-C=O and CO_3^{2-} environments respectively.[50] Those species are assigned to adventitious carbon usually identified at the material surface. The O1s spectra exhibit a component at around 529.2 - 529.4 eV corresponding to O^{2-} anions in the NMC crystalline network and two other components located at 531.7 eV and 534.6 eV attributed to CO_3^{2-}/O-C=O/C=O and C-O environments.[50] In the 45-80 eV binding energy range, Ni3p, Co3p, Li1s and Mn3p core peaks have been identified and located at 68.1 eV (Ni^{2+}/Ni^{3+})[51], 61.2 eV (Co^{3+})[52], 54.2 eV (Li)[52] and 49.9 eV (Mn^{4+})[51]. Those peaks were chosen to perform a more precise quantitative analysis as they are in the same binding energy range as opposed to the 2p core peaks. The Li1s peak is decomposed into two components at 54.2 eV and 55.6 eV attributed to Li^+ ions in the NMC crystalline network (labelled Li_{NMC}) and in Li_2CO_3 (labelled Li_2CO_3)[53], respectively. From these spectra, quantitative analyses were performed in order to compare the surface compositions of these three samples. The results, displayed in atomic percentages, are summarized in **Table 2** and **Table 3** for the three compounds. As an example, the complete quantitative analysis of the 810-5-O_2 material can be found in **Table S3.** Only the most interesting values obtained from these quantitative analyses are discussed hereafter. In **Table 2** the atomic percentages, extracted from global quantification, are given for the Li and C coming from Li_2CO_3 contributions and for the oxygen atoms in the NMC network (O_{NMC}). The samples 810-5-O_2 and 900-5-O_2 are those that show the lowest carbonate proportions at their surface, and thus the highest proportions of transition metals and oxygen from the layered oxide (NMC), as less covered. The sample 930-5-O_2 shows a higher proportion of Li_2CO_3 detected at the surface and thus less transition metals and oxygen from the layered oxide. Note that the detection of Li_2CO_3 by XPS surface characterization (with an analysis depth of 5-10 nm), despite not detected by XRD, allows explaining the overlithiation results obtained by ICP-OES and CHNS chemical analyses. In addition, it is worth mentioning that there is no relationship between the quantity of Li_2CO_3 measured at the surface and the amount of Ni^{2+} ions in the interslab spaces as determined by the Rietveld refinement. Indeed, the samples have very similar amounts of Ni^{2+} ions in the interslab spaces (between 1.5 and 1.8%, as shown in **Table 1**) but different amounts of Li_2CO_3 at their surface. The results in **Table 3** confirm the transition metal stoichiometry on extreme surface for the materials. All samples are characterized by a stoichiometry Ni:Mn:Co close to 6.7:1.6:1.7 at the surface versus 6:2:2 in the bulk, showing that the composition at the surface is enriched in Ni versus Co and Mn.

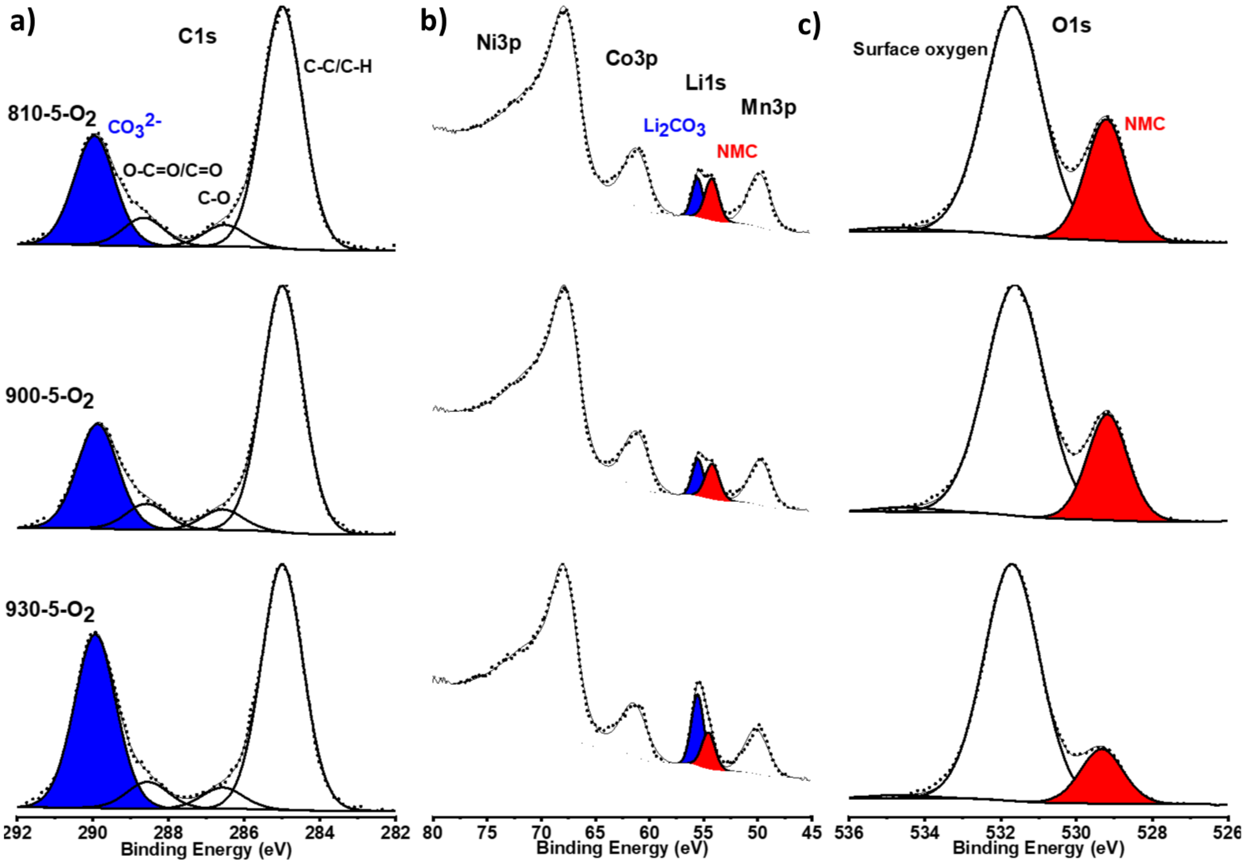

Figure 3. C1s (a), Ni3p-Co3p-Li1s-Mn3p (b) and O1s (c) XPS spectra of the three active materials. The C_{CO_3} and $Li_{Li_2CO_3}$ peaks are highlighted in blue and the O_{NMC} and Li_{NMC} peaks are highlighted in red. The dots and the lines represent the experimental and the fitted data respectively.

Table 2. Comparison of the contribution of the carbonate species in the C1s and Li1s spectra, and the contribution of oxygen from the electrode material in atomic percentages extracted from the global quantitative analyses performed from XPS spectra of the materials.

	Atomic percentages		
Samples	**C (Li_2CO_3)**	**Li (Li_2CO_3)**	**O_{NMC}**
930-5-O_2	9.1	19.2	6.8
900-5-O_2	6.3	12.7	9.7
810-5-O_2	6.2	13.0	10.1

Table 3. Transition metal ratios obtained from Ni, Mn and Co atomic percentages extracted from the global quantitative analyses of the XPS spectra collected for the three compounds.

	Atomic percentages				
Samples	**Ni 3p**	**Mn 3p**	**Co 3p**	**ΣTM**	**(Ni:Mn:Co)/ΣTM**
930-5-O_2	4.1	1.0	1.0	6.1	0.67 : 0.16 : 0.16
900-5-O_2	5.8	1.3	1.4	8.5	0.68 : 0.15 : 0.16
810-5-O_2	5.8	1.5	1.6	8.9	0.65 : 0.17 : 0.18

Electrochemical analyses

These three NMC622 powders were electrochemically tested in CR2032 type coin cells versus Li metal in galvanostatic mode, either in an organic liquid electrolyte or in a gelified electrolyte, in the same cycling conditions, at room temperature and in the 2.5-4.3V vs. Li^+/Li potential range. First, three formation cycles were performed at room temperature: the first at C/20 (1 charge and 1 discharge in 20 hrs), the second at C/10 and the third at C/5. Then, the samples were cycled at C/5 in the same potential range, with a constant voltage step at 4.3V at the end of every charge until the current becomes smaller than that corresponding to C/85. **Figure 4** shows the charge-discharge curves obtained for the three compounds during the 1st formation cycle at C/20 (**Figure 4a**) and the 4th cycle at C/5 (i.e. that corresponding to the 1st cycle after the three formation cycles) (**Figure 4c**), in both types of electrolytes. The corresponding dQ/dV=f(V) curves are given in **Figures 4b** and **4d**, respectively. As highlighted by the cycling curves given in **Figure 4** and in **Figure S2** (in supplementary information for that latter), the duration of the constant voltage step increases with the size of the particles and when cycling is performed in gelified electrolyte. The discharge capacity and irreversible capacity (IRCs) obtained at the end of the 1st cycle, as well as the discharge capacity obtained during the 4th cycle are gathered in **Table 4**, for the three electrode materials and the two types of electrolytes. The evolution in performances according to changes in the particles' size is similar in both types of batteries, using a liquid organic electrolyte and a gelified electrolyte. The performance tends to decrease with the increase of the particles' size on one side and in gelified electrolyte versus the conventional organic liquid electrolyte on the other side, as highlighted especially in **Figures 4c-d** by increasing voltage polarization for larger particles' sizes and even more in gelified electrolyte. The larger the polarization, the longer is the duration of the constant voltage step. Beyond these observations, it is worth mentioning that the performances are very similar for the powders showing 240 and 810 nm particles' sizes (the samples 810-5-O_2 and 900-5-O_2, respectively) in the conventional liquid electrolyte. Furthermore, the 240 nm primary particles deliver the best and similar performances in both electrolytes: a discharge capacity of ~182 mAh/g and an IRC of ~6.5%. Increasing the particle size tends to decrease the interfacial area with the conventional electrolyte and thus limit the parasitic reactions. Nevertheless, in parallel it implies also larger diffusion path for Li^+ ions within the solid. An optimum has thus to be found for the primary particle size to deliver the highest reversible capacities and best capacity retentions regardless of the cycling rate: here it appears to be 240 nm for good performances both in conventional liquid and in gelified electrolytes whereas 810 nm shows similar performance only in liquid electrolyte.[42] This result obtained for 810 nm particle size suggests that the wettability by the gelified electrolyte is much difficult as the particle size increases.

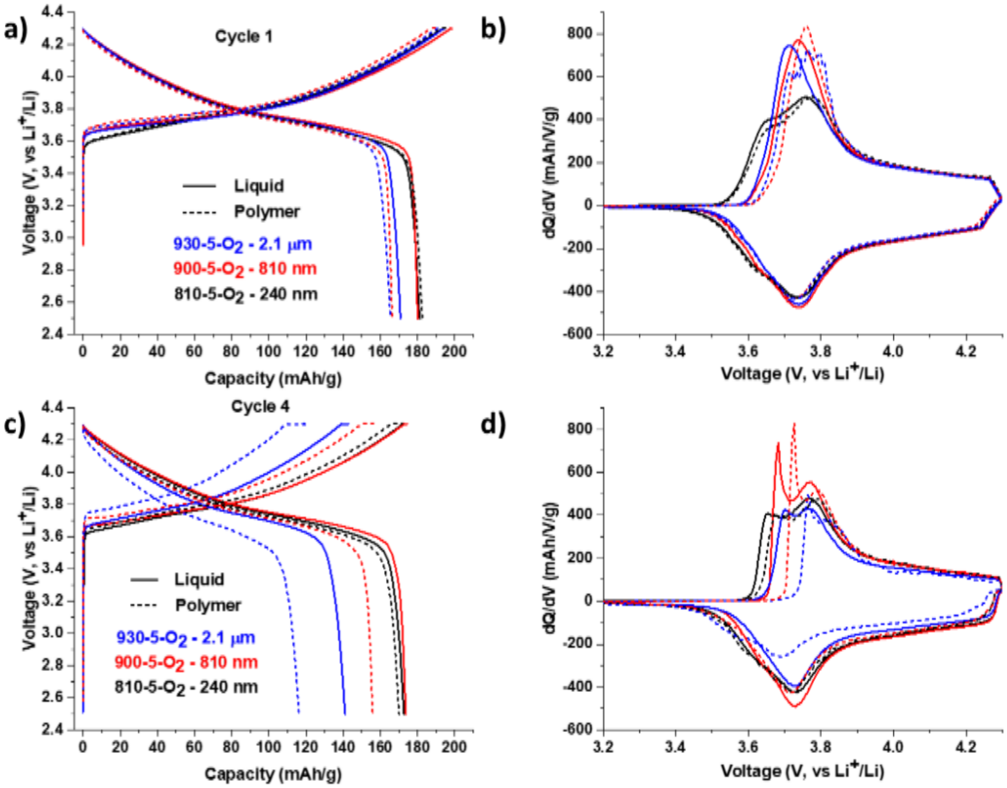

Figure 4. Charge-discharge curves of the three samples cycled in a conventional organic liquid electrolyte and in a gelified electrolyte: 1st cycle (a) and 4th cycle (c). Corresponding dQ/dV=f(V) curves for the 1st cycle (b) and the 4th cycle (d). The samples underwent three formation cycles at C/20, C/10 and C/5 and were then cycled at C/5 in the potential window 2.5-4.3V vs. Li^+/Li. The potential is maintained at 4.3V until the current becomes smaller than that corresponding to C/85, at the end of every charge.

Table 4. 1st and 4th discharge capacities and irreversible capacities percentage (IRC, %) obtained upon cycling of the 3 samples versus Li metal in conventional organic liquid and gelified electrolytes.

			C/20 ; 2.5-4.3V, 1st formation cycle				**C/5 ; 2.5-4.3V, cycle 4**	
			Liquid electrolyte		**Gelified electrolyte**		**Liquid electrolyte**	**Gelified electrolyte**
Sample	**%Ni$_{Li}$**	**Average primary particle size**	**Discharge capacity (mAh/g)**	**IRC (%)**	**Discharge capacity (mAh/g)**	**IRC (%)**	**Discharge capacity (mAh/g)**	**Discharge capacity (mAh/g)**
930-5-O$_2$	1.8	2.1 µm	171	12	165	14	141	116
900-5-O$_2$	1.5	810 nm	180	9	166	13	174	156
810-5-O$_2$	1.8	240 nm	181	7	183	6	173	170

Figure 5 shows the evolution of the discharge capacities delivered by the 3 samples after a larger number of cycles, 53 cycles were performed in the gelified electrolyte and 105 cycles in the conventional organic liquid electrolyte. **Figure 5** reveals that the reversible discharge capacity decreases continuously upon cycling of the three samples, whatever their particles' size, in the conventional electrolyte, with a loss of capacity smaller than 36% after 100 cycles and in good agreement with the results we recently reported.[42] When cycled in the gelified electrolyte, much lower performances are obtained as already discussed, with a first rapid drop during the first three cycles and a second rapid drop of the reversible discharge after less than 50, 30 and 20 cycles for the 810-5-O$_2$, 900-5-O$_2$ and 930-5-O$_2$ samples respectively as highlighted in **Figure 5** and in **Figure S3** (given in supplementary information for that latter). It is interesting to highlight that despite the cycling is performed at room temperature and at a rather fast rate of C/5, performances are similar in gelified electrolyte and in conventional organic liquid electrolyte for the sample 810-5-O$_2$ with 240 nm particles' size during the 40 first cycles.

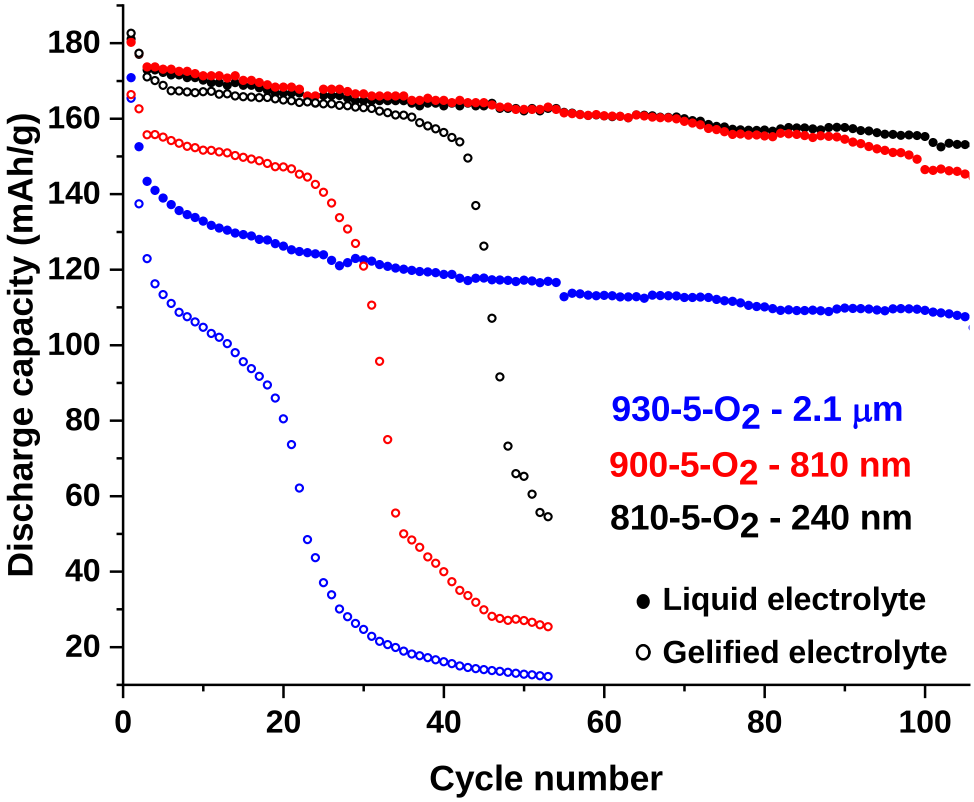

Figure 5. Evolution of discharge capacities delivered by the 3 samples cycled versus Li metal in conventional organic liquid and gelified electrolyte. The samples were cycled at a C/5 rate, in the potential window 2.5-4.3V after 3 formation cycles at C/20, C/10 and C/5. A constant voltage step is performed at end of every charge until the current becomes smaller than that corresponding to a C/85 rate.

In order to get more insight into the reactivity of the 3 materials, showing different particle sizes ranging between 240 nm and 2.1 μm, different analyses were carried out to characterize the electrodes recovered after cycling in both types of electrolytes: after 10 cycles (after the 3 formation cycles) and after 105 (or 53) cycles at the end of the charge (EOC) or of the discharge (EOD). OCV electrodes, exposed to the electrolyte without cycling, were also studied for comparison. They were first observed by SEM to compare their morphologies and determine if some of them contained more fractures than others, that could reflect more important mechanical strains. The morphology of the electrodes was first investigated by scanning electron microscopy. The electrodes were then characterized by XPS analyses to study the electrode/electrolyte interface composition.

Electrodes morphology analysis after cycling

As shown in **Figure S4 (left)** the morphology of the agglomerates made of 2.1 µm or 240 nm size particles is not affected after cycling in the conventional electrolyte, showing that the particles and the agglomerates keep good integrity and that the large number of cycles doesn't have a significant impact on their morphology. Nevertheless, when observing the electrodes at lower magnification, the electrodes made with 240 nm size particles (**Figure S4g-i left**) seem to become slightly more porous after cycling, however these observations were made on electrodes after being separated from the separators with possible removal of electrode parts. These 240 nm particles seem to be also covered by a thick layer after 10 or 105 cycles compared to the OCV ones (**Figure S4j-l left**). **Figures S4d-f (left)** suggest that no cracks are observed within the large 2.1 µm size particles after 10 or 105 cycles in liquid electrolyte, even in the charge state (EOC) of the battery, in good agreement with the composition of the layered oxide NMC622 and with the potential window limited to 4.3V vs Li^+/Li. Indeed, intragranular cracks were previously observed in NMC 811 layered oxides, richer in Ni and prone to undergo huge volume variations in the highly deintercalated state,[53-56] and especially in a wider potential window (≥ 4.45V vs Li^+/Li).[57-58] The same comparison is made for electrodes cycled in the gelified electrolyte in **Figure S4 (right)**. As shown especially in **Figures S4d-f (right)**, a part of the gel remains within the electrodes even after the washing protocol making difficult to figure out if cracks are formed within the large 2.1 µm size particles after 10 or 50 cycles in the potential window 2.5-4.3V vs Li^+/Li. The electrodes appear to keep good integrity after their cycling in gelified electrolyte, as in the conventional organic liquid electrolyte. As the formation of the gel is performed after assembling the cell, the electrolyte in its liquid state fills the porosity of the electrodes as well as that of the separator, and then the increase of the temperature to 60°C allows creating an interpenetrated network of the gel electrolyte within the solid-state batteries. In order to get more insight into the volume of the electrodes, cross sections were analysed by SEM.

Figure 6 compares cross sections of electrodes made with 2.1 µm and 240 nm particles, after their contact with a conventional organic liquid electrolyte (left side of the figure) and with a gelified electrolyte (right side of the figure). **Figure 6** gives the comparison of the pristine state before cycling, with that observed at the end of the charge after 105 (or 50) cycles. These cross sections allow showing a good distribution, on the left of the PVdF binder, carbon black and active material in the volume of the electrodes, and on the right of the same components with in addition the gelified electrolyte. As shown in **Figure S5** given in supplementary information, it appears that the penetration of the gel is probably not achieved in the intergranular spaces (red arrows) within the aggregates of large 2.1 µm size particles, whereas it is for 240 nm size particles (**Figure 6c-f right**). It could be one of the origins of the lower performance of the 930-5-O_2 sample (2.1 µm size particles) in all these solid-state batteries (**Figure 5**). Indeed, this smaller "wettability" by the gelified electrolyte induces, combined with larger particle sizes, diffusion limitations.[59]

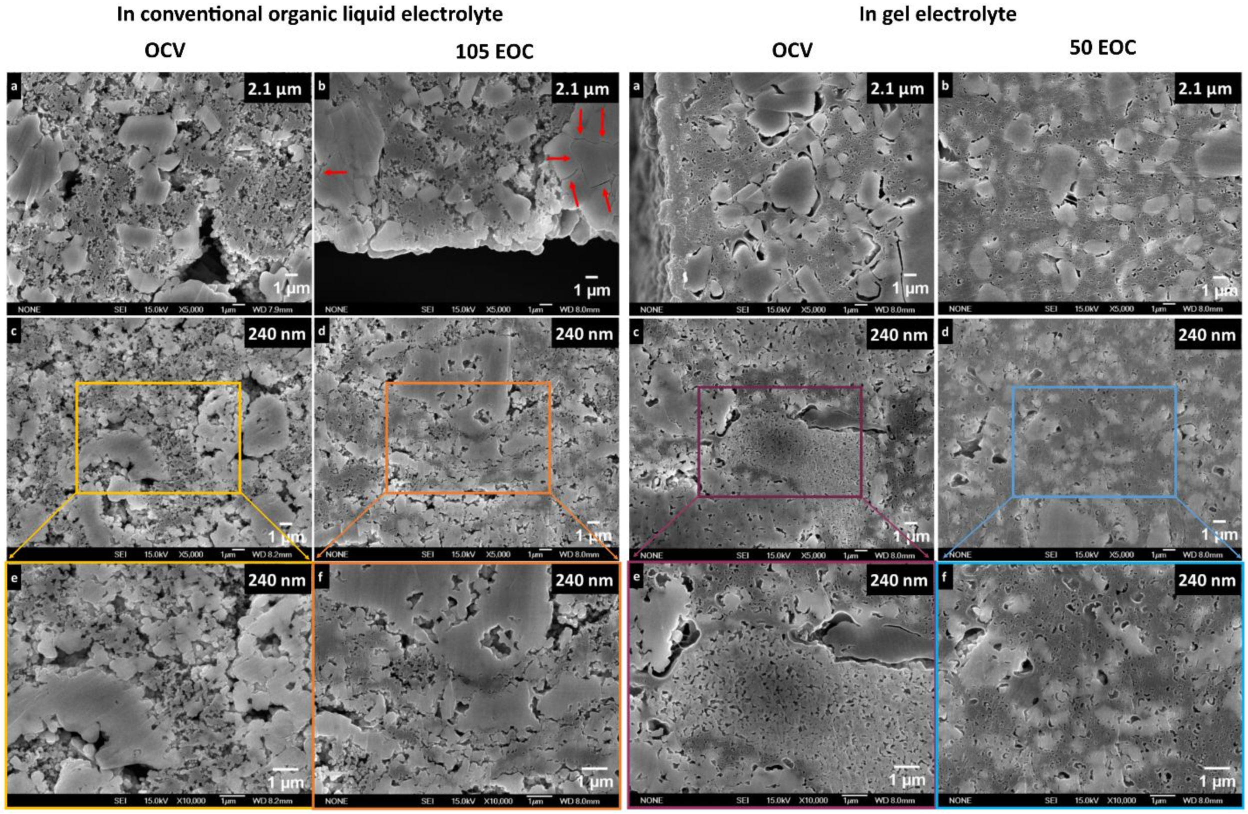

Figure 6. Observation by SEM of cross sections of electrodes after being put in contact with the electrolyte (conventional organic liquid electrolyte on the left and gelified electrolyte on the right): in the pristine state without cycling (OCV) (a, c, e) and after 105 (or 50) cycles at the end of the charge (EOC) (b, d, f). SEM images of electrodes made with 2.1 µm size particles (a, b) and 240 nm size particles (c and d, and their magnification in e and f respectively) are compared. The red arrows emphasize intergranular spaces in the aggregates of the 2.1 µm primary particles after cycling in liquid electrolyte (also seen after cycling in gel electrolyte in **Figure S4**).

XPS analysis of the positive electrode/electrolyte interface after cycling

XPS analyses were performed on these electrodes made from the 930-5-O_2 (2.1 µm particles), 900-5-O_2 (810 nm particles) and 810-5-O_2 (240 nm particles) samples after their cycling in the conventional organic liquid electrolyte and in the gelified electrolyte, in order to compare the nature of the interface. Electrodes were analysed after being exposed to the electrolyte without cycling (OCV), after 10 cycles at the end of charge and discharge (10 EOC and 10 EOD respectively) and after 105 (or 50) cycles at the end of charge and discharge (105 (50) EOC and 105 (50) EOD respectively). Pristine electrodes were also analysed for comparison. The comparison of all these XPS spectra is given in **Figure 7**, as an example for the 810-5-O_2 sample showing 240 nm particles. The results obtained from the quantitative analysis of the spectra collected for the 810-5-O_2 electrode recorded after 10 cycles at the end of the charge (810-5-O_2 - 10 EOC liq) are given in details in **Table S4** as an example.

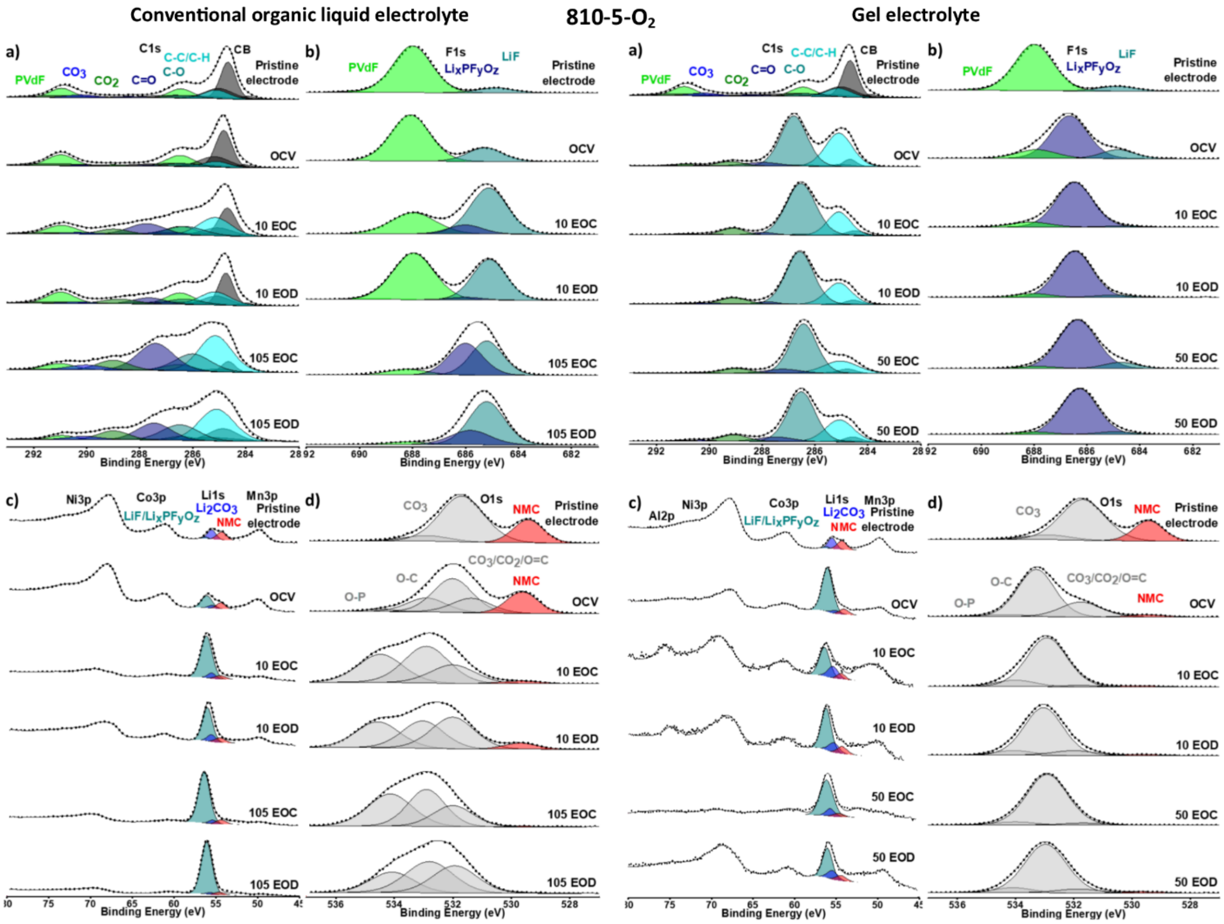

Figure 7. C1s (a), F1s (b), Li1s, Ni3p, Co3p, Mn3p (c) and O1s (d) XPS spectra collected for electrodes made of 240 nm particles (810-5-O_2 sample) cycled in the conventional organic liquid electrolyte (left) and in the gelified electrolyte (right). The spectra obtained after 10 cycles and 105 (or 50) cycles at the end of charge and discharge are compared to those obtained for the pristine and OCV electrodes. The dots and the lines represent the experimental and the fitted data respectively.

As the two types of electrolytes (organic liquid and gelified) contain $LiPF_6$ as salt and carbonate-type constituents, the compounds expected to compose the degradation layer localized at the interface between the electrode and the electrolyte are the same as those already identified in our recent work on these NMC622 type compounds[42]: LiF and $Li_xPF_yO_z$-type species, as well as carbonaceous and oxygenated species. We thus focused on the analysis of the C1s, F1s, Li1s, Ni3p, Co3p, Mn3p and O1s XPS spectra as their combination allows getting more insight into the degradation of the solvents and of the salt, but also on the degree of coverage of the pristine electrode by degradation products.

In good agreement with the presence of additives (carbon black and binder) additional components are observed in the spectrum of the pristine electrode versus that given in **Figure 3** for the powder. In the C1s spectra, two contributions located at 286.5 eV and 291.0 eV were attributed to CH_2 and CF_2 chemical environments of the PVDF binder, respectively. The signature of the carbon black in the electrode is also well characterized by a set of black peaks, represented in **Figure S6**. The F1s spectrum is composed of two contributions, one from the PVDF binder located at 688.0 eV and attributed to the CF_2 environments and a very small contribution at 685.2 eV attributed to LiF.[60-61] A new component also appears at 56.1 eV under the Li1s peak according to LiF species. In comparison with the **Figure 3**, we can note a decrease of the contribution of the O_{NMC} component (from 30% to 20%) in the whole O1s spectrum corresponding to the presence of oxygenated species coming from the electrode formulation.

Cycling in the conventional organic liquid electrolyte

After OCV, the contribution of LiF in the F1s spectrum slightly increases, which is correlated with the increase of the component at 56.1 eV under the Li1s peak according to LiF species. The oxygen function linked to solvent degradation like CO_2 or O=C species on one side and to C-O species[60-61] on the other side are associated to the peaks at 531.9 eV and 532.9 eV, respectively.

A very light amount of phosphate species has been also deposited after OCV (less than 1 at%). No either modification has been reported.

Now, we follow the evolution in the core peaks spectra associated to the deposition of species on the electrode surface upon cycling at different stages in the conventional organic liquid electrolyte (**Figure 7-left**), especially to investigate the impact of the particles size on the degradation products and the covering of the electrodes.

In the F1s spectra, the cycling is concomitant with the appearance of a third component at 686.1 eV associated to the deposition of $Li_xPF_yO_z$ species, which is more quantitative for the 810-5-O_2 sample. We also note a large increase of the LiF component, coming from the electrolyte salt decomposition. Concomitantly, a corresponding increase of the LiF/$Li_xPF_yO_z$ component in the Li1s spectra at 56.2 eV is observed.

The O1s and C1s spectra are also modified after cycling, due to the degradation of electrolyte salt and solvents. For O1s spectra, the O_{NMC} component at 529.6 eV tends to disappear (from 20% to 2% of the O1s signal) while the contribution of the components at higher binding energy (532.0 eV, 533.0 eV and 534.3 eV) is continuously increasing as the covering increases along the cycling. The formation of oxygenated fluorophosphates species corresponds to the peak at 534.3 eV.

All along the cycling, the contributions in the C1s spectra located at 285.1, 286.4, 287.5 and 288.9 eV assigned to C-C/C-H, C-O, C=O and O-C=O environments respectively are increasing according to the solvents degradation. From the direct observation of these spectra, we can easily detect a slight consumption of the degradation species at the end of each discharge.

The comparison of the results obtained for the three materials cycled in the conventional organic liquid electrolyte are summarized in **Figure 8a-c** and in **Table S5**. Only the most interesting values obtained from those quantitative analyses are discussed hereafter. The atomic percentages contribution of each element associated to electrode components and degradation species are gathered into three different categories: carbon black; LiF/$Li_xPF_yO_z$ species containing the LiF and $Li_xPF_yO_z$ contributions in Li1s and F1s and the phosphate contributions; and carbonaceous species comprising the remaining contributions in C1s spectra (i.e. contributions that are not carbon black nor PVDF), the remaining contributions in O1s spectra (i.e. contributions that are not NMC nor phosphate species) and the Li_2CO_3 contribution in Li1s spectra.

First, the amount of LiF/$Li_xPF_yO_z$ species is increasing along the cycling reflecting an important degradation of the $LiPF_6$ at the surface. We note a significantly larger amount of those species at the surface of the 240 nm particles (810-5-O_2 sample) especially after 105 cycles. The salt degradation is decreasing as the particles size is increasing (after 105 cycles at the end of charge: 64.6 at.% for the 810-5-O_2, versus 45.4 at.% for the 900-5-O_2 and 42.6 at.% for the 930-5-O_2 samples). Consequently, the evolution of the carbon black and carbonaceous species surface composition is affected as the amount of those two species are less observed for the sample with smaller particles (810-5-O_2 sample).

We found that the atomic percentages of carbonaceous species are increasing with the particles size and along the cycling. For example, after 105 cycles at end of charge, we report 25.7 at.%, 38.0 at.% and 40.4 at.% for, respectively, the 810-5-O_2 (240 nm particles), 900-5-O_2 (810 nm particles) and 930-5-O_2 (2.1 μm particles) samples.

For the carbon black (CB), the tendency is an increase of its covering by the SEI during cycling; this covering being thicker for smaller particles (1.6 at.% for the 240 nm particles after

105 cycles at end of charge for example, versus 7.9 at.% and 8.1 at.% respectively for the 810 nm particles and the 2.1 µm particles).

We thus identify that the covering of the electrode material by the SEI is less important for larger particles as for the 930-5-O_2 sample (2.1 µm). As shown in one of our previous works, the increase of particle size allows the decrease of the specific surface area which limits the parasitic reactions at the electrode/electrolyte interface, thus reducing the amount of degradation products formed in the SEI and limiting the covering of the electrode.[42] These XPS results show that the amount of $LiPF_6$ and solvents degradation products deposited at the surface of the electrodes during cycling depends on the particles size, i.e., the degradation products of the $LiPF_6$ are much more represented in the SEI of smaller particles electrode material whereas the SEI of larger particles electrode material contain a larger proportion of solvents degradation products.

Cycling in the gelified electrolyte

The C1s, F1s, Li1s, Ni3p, Co3p, Mn3p and O1s XPS spectra obtained for the 810-5-O_2 electrodes after their cycling in the gelified electrolyte are shown in **Figure 7-right** as an example. The spectra were decomposed in the same way as previously described. The complete quantitative analysis achieved for the spectra collected for the 810-5-O_2 electrode recovered after their cycling for 10 cycles and at the end of the charge (810-5-O_2 - 10 EOC gel) are given in **Table S6** as an example. The results obtained from those analyses are compared for the three samples in **Figure 8d-f** and in **Table S7**, as for those obtained in the conventional organic liquid electrolyte. Moreover, we can notice, for some electrodes, a slight content (< 1 at. %) of Aluminium and/or Magnesium, which origin is not known.

We remark that, for the three materials, a much larger quantity of carbonaceous species (especially C-O species located at 286.6 eV) was found at the surface of the electrodes, regardless of the particles morphology, as soon as they were exposed to the electrolyte (from 24.3 ± 1.0 at.% for the pristine electrodes to 69.0 ± 2.5 at.% for the OCV electrodes). This could be explained by the thin layer of gel, observed by SEM (**Figures S4d-f** and **S4j-l**), which remains at the surface of the electrodes after DMC washing. Thus, the components associated to the electrode material (O_{NMC}, C_{PVdF}, F_{PVdF} and CB) are very quickly not discernible anymore on the XPS spectra. As an example, the carbon black contributions are decreasing from 36.7 ± 2.2 at.% for the pristine electrodes to 2.5 ± 1.8 at% for the OCV electrodes (**Table S7**).

In that condition, we can only investigate the $LiPF_6$ degradation of the gelified electrolyte along the cycling regarding the particles size of the NMC622 electrodes.

For the cycled electrodes, we notice that the amount of carbonaceous species, mainly coming from the remaining gel layer at the surface of the electrodes, remains high (62.5 at.%, 48.2 at.% and 54.1 at.% for, respectively, the 810-5-O_2, 900-5-O_2 and 930-5-O_2 samples, at end of charge of the 50th cycle for example) but varies between the different states of charge (between 67.5 ± 5.0 at.%, 59.9 ± 11.7 at.% and 61.2 ± 9.8 at.% for respectively the 810-5-O_2, 900-5-O_2 and 930-5-O_2 samples) showing that its thickness may not be constant between the different electrodes.

The proportion of carbon black species remains very low for the three materials, regardless of the state of charge (4.0 at.%, 0.9 at.% and 0.8 at.% for, respectively, the 810-5-O_2, 900-5-O_2 and 930-5-O_2 samples, at end of charge of the 50th cycle for example), showing that the electrodes are all covered in a similar way by the degradation products and the remaining gel layer.

Although the degradation products may be hidden by the remaining gel layer at the surface of the electrodes, the proportions of LiF/$Li_xPF_yO_z$ species are similar after 10 or 50 cycles and increase less sharply than for the liquid electrolyte (18.9-31.1 at.%, 24.9-47.4 at.% and 21.9-40.9 at.% for respectively the 810-5-O_2, 900-5-O_2 and 930-5-O_2 samples) showing a probable more moderate degradation of the $LiPF_6$ at the surface and a relatively stable electrode/electrolyte interface. The results exhibit a lower degradation of the polymer electrolyte for the 240 nm particles sample regardless of the cycle number and state of charge according to the atomic percentages evolution of the $LiF/Li_xPF_yO_z$ species (31.1 at.%, 47.4 at.% and 40.9 at.% for, respectively, the 810-5-O_2 (240 nm particles), 900-5-O_2 (810 nm particles) and 930-5-O_2 (2.1 µm particles) samples, at end of charge of the 50th cycle for example).

Those results show that, for very different particles size from 240 nm to 2.1 µm, the composition of the electrode/gel electrolyte interface does not differ much from one material to another. The nature of the degradation products is not very different either from those observed in the liquid electrolyte so it cannot explain the capacity drop observed for the 3 samples after a given number of cycles (**Figure 5**). Also, as the SEI compositions after 50 cycles, i.e. after the capacity drop, is not that different from those after 10 cycles, this rapid capacity drop may not be caused only by the degradation of the electrolyte on the positive electrode side. The reactivity of the gel versus the Li metal electrode and the possible formation of Li dendrites have to be considered to explain this capacity drop. Further studies are needed to better understand the reactivity between the Li metal negative electrode and the gel electrolyte. To this end, a similar study of the Li metal negative electrode/gel electrolyte interface at different states of charge along cycling, like the one we performed on the positive electrode side, could be interesting to perform.

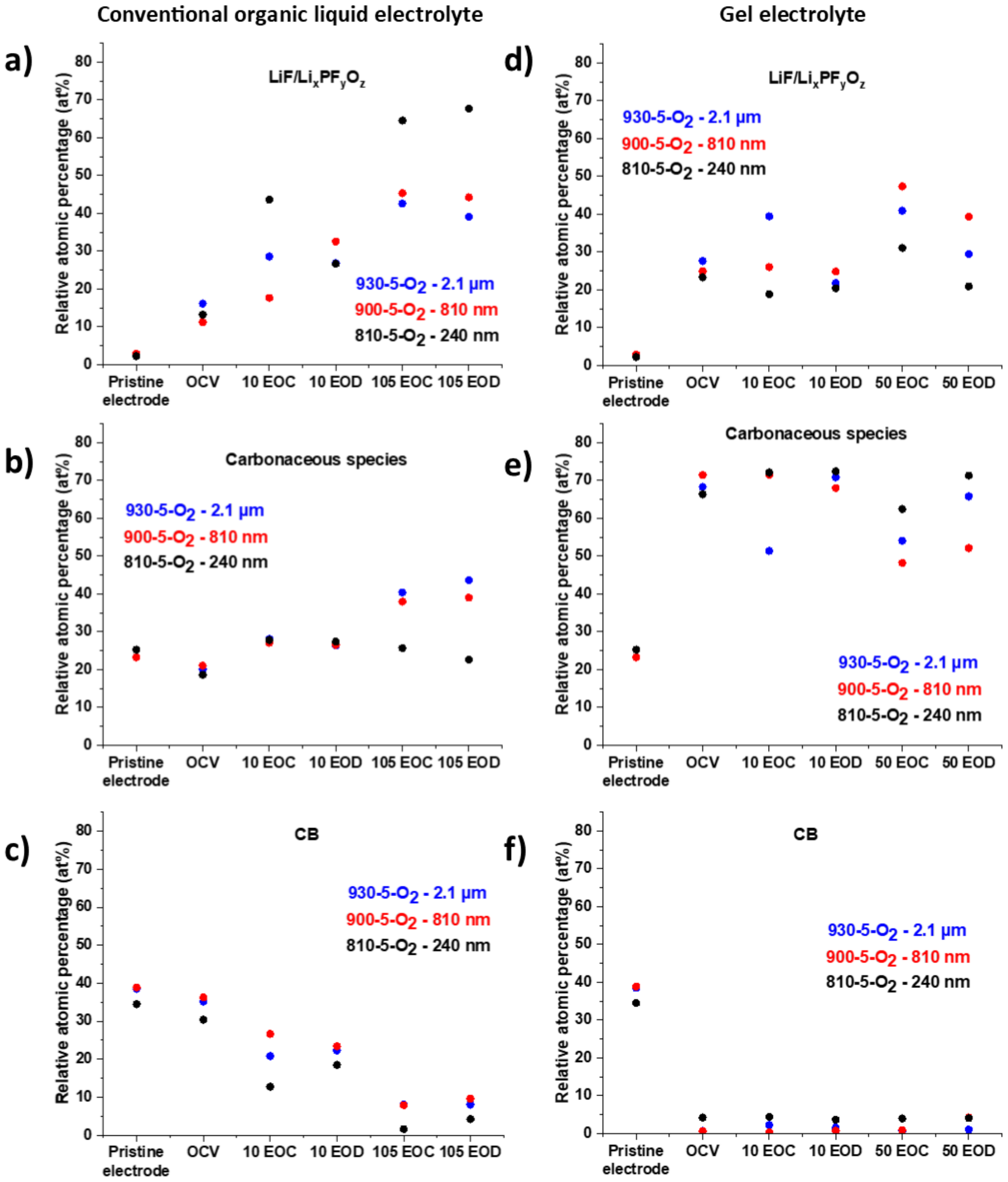

Figure 8. Evolution of the amount of LiF/$Li_xPF_yO_z$ species (a, d), carbonaceous species (b, e) and carbon black (CB) proportions (c, f) depending on the state of charge and discharge in the conventional organic liquid electrolyte (a-c) and in the gelified electrolyte (d-f). These amounts were determined from the quantitative analyses of the XPS spectra collected for the 240 nm (black dots), 810 nm (red dots) and 2.1 µm size particles (blue dots).

To support the hypothesis that the reaction between the gelified electrolyte and the lithium metal electrode is responsible for the capacity drop, a complementary cycling test was performed in the gelified electrolyte with an 810-5-O_2 electrode (240 nm particles). As shown in **Figure 9**, a coin cell was cycled in the same conditions as those previously described (C/5 rate; in the potential window of 2.5-4.3V vs. Li^+/Li after 3 formation cycles at room temperature at C/20, C/10 and C/5) until the capacity drop occurs after 53 cycles. It was dismantled, the positive electrode was recovered, washed with DMC and put back in a new coin cell with a new separator and Li negative electrode, to see if the performances could be improved or recovered when the Li metal/gelified electrolyte interfaces are renewed. The first discharge capacity obtained in the new coin cell is significantly improved compared to the discharge capacity delivered at the end of the previous cycling: 126 mAh/g vs. 52 mAh/g. This shows that renewing the Li metal/gelified electrolyte interfaces has a significant beneficial effect over the electrochemical performances so the reactivity at the negative electrode side has an actual impact on the capacity drop observed for the 3 samples. However, the capacity delivered by this new coin cell is still far from that obtained at the beginning of the pristine cycling: 126 mAh/g vs. 173 mAh/g, meaning a 27% decrease of the 1st discharge capacity between the pristine and the second cycling. Indeed, as shown by the SEM analyses previously discussed, a residual gel electrolyte layer remains at the surface of the positive electrode even after being washed with DMC. So, on the contrary to the Li metal/gelified electrolyte interface, that of the positive electrode with the electrolyte could not be renewed. Even if the residual gel electrolyte could have retained a part of the CEI of the positive electrode, it is not obvious that the second polymerization creates an actual continuity with the residual gel, thus limiting the possibilities for lithium diffusion and explaining the improved, but mitigated, electrochemical properties of this renewed battery.

One of the possible strategies to stabilize the interface with the Li metal and prevent the Li dendrites growth into the gel electrolyte is to improve the mechanical properties of the polymer matrix by synthetizing a composite, often by adding ceramic fillers for example ($Li_7La_3Zr_2O_{12}$ (LLZO), $Li_{6.75}La_3Zr_{1.75}Ta_{0.25}O_{12}$ (LLZTO), $Li_{0.35}La_{0.55}TiO_3$ (LLTO)…).[62–70] The idea is to give the gel, on one hand, a high hardness to prevent the Li dendrites from penetrating inside the electrolyte and, on the other hand, a shear modulus at least twice as high as the one of Li metal (> 8 GPa) to avoid increasing the surface roughness at the Li/electrolyte interface that would enhance the Li dendrites growth through the electrolyte.[23,71] Another way to decrease the reactivity between the Li and the gelified electrolyte could be to synthesize a surface layer to stabilize the Li metal/electrolyte interface, prevent the electrolyte degradation and maintain a good contact and conductivity at the interface.[72] Different kinds of surface layers can be formed: alloy interfacial layers (based on Al[73-74], Si[75], Ge[76-77], Sn[78-79], Au[80] for example), polymer layers (based on CPMEA ((polyethylene glycol)methyl ether acyalte)[81], PEO (poly(ethylene oxide))[82], PAN (poly(acrylonitrile))[83], PEGDA (poly(ethylene glycol diacrylate))[84] for example), LiPON (lithium phosphorus oxynitride)[85] or LiF[86-87].

This study has revealed that, despite undergoing similar degradation phenomenon, induced mostly by the reactivity between the gelified electrolyte and the negative electrode, the morphology of the positive electrode material plays an important role in those degradation reactions. Degradation reactions are mitigated for smaller particles' sizes, promoting longer cyclability and better performance.

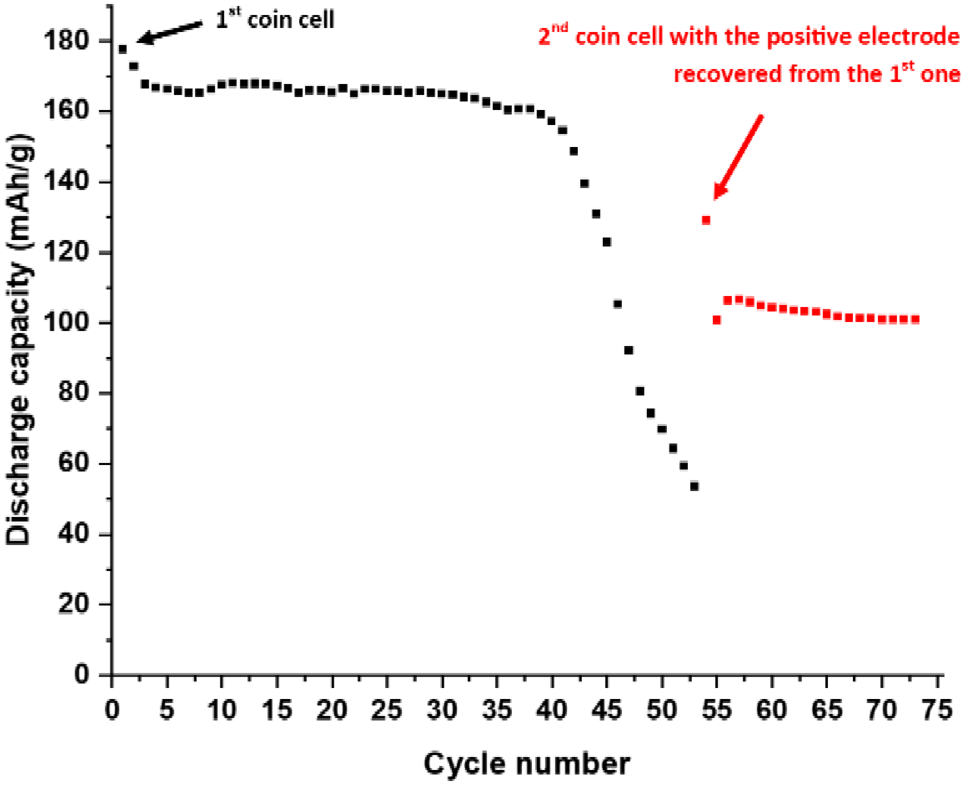

Figure 9. Electrochemical performances of an electrode made of the 810-5-O_2 (240 nm particles) sample and cycled in the gelified electrolyte. One first coin cell was cycled (black squares) and dismantled after the capacity drop after 53 cycles, the positive electrode was recovered and reintroduced in a new coin cell (red squares).

CONCLUSION

Three NMC622 type layered oxide samples, with crystallographic structure close to the ideal 2D layered structure (less than 2% Ni^{2+} ions in Li^+ sites) and with different primary particle sizes of 240 nm, 810 nm and 2.1 μm, were obtained. They were tested in coin cells vs. Li metal in a conventional organic liquid electrolyte and in a gelified electrolyte, both containing $LiPF_6$ as salt and carbonate type constituents. Their electrochemical performance and surface reactivity at the interface with the electrolytes were compared to identify a possible effect of the primary particle size. In the liquid electrolyte, the 240 and 810 nm particles showed good performances upon long range cycling, whereas the 2.1 μm particles showed limited performance due to diffusion limitations. Despite a larger quantity of $LiF/Li_xPF_yO_z$ species reflecting a more important $LiPF_6$ degradation in the liquid electrolyte for the 240 nm particles, induced by their larger interfacial area, it is not detrimental to their performance. Only these 240 nm particles show similar performance in both electrolytes, despite a rapid loss of cyclability in the gelified electrolyte after few tens of cycles. For larger particles of 810 nm and 2.1 μm in diameter, limited discharge capacity is observed in the gelified electrolyte versus the conventional organic liquid one, with a capacity drop after a more limited number of cycles compared to the 240 nm particles. Lower amounts of $LiF/Li_xPF_yO_z$ species were found at the surface of the 240 nm particles, regardless of the state of charge, reflecting a less important $LiPF_6$ degradation compared to the 810 nm and 2.1 μm particles. Smaller particles' sizes promote longer cyclability and better performance in both electrolytes. The similar compositions of the positive electrode/gel electrolyte interfaces between the three materials and between the beginning and the end of the cycling suggest the role played by the reactivity between the Li metal negative electrode and the gel electrolyte in these performances drops. Indeed, the recovery of a significant part of the electrochemical performances lost after the capacity drop was observed after renewing the Li metal/electrolyte interfaces. Those results suggest that the reactivity between the gelified electrolyte and the negative electrode is mostly responsible for this capacity drop observed for the three materials and that the morphology of the positive electrode material plays an important role in the degradation reactions occurring at the interface. Further studies are needed to better understand the reactivity between the gel electrolyte and the Li metal negative electrode in order to improve the performances of the batteries containing this gel electrolyte.

ASSOCIATED CONTENT

Supporting information

The Supporting information contains Figures, Tables and description to complete and precise some points in the main manuscript. This material is available free of charge via the Internet at http://pubs.acs.org.

AUTHOR INFORMATION

Corresponding author

* Laurence Croguennec

Laurence.Croguennec@icmcb.cnrs.fr

* Delphine Flahaut

delphine.flahaut@univ-pau.fr

Funding Sources

This work was funded by Saft and Région Nouvelle Aquitaine.

ACKNOWLEDGMENT

The authors acknowledge Saft and Région Nouvelle-Aquitaine for the funding of the project, as well as the French National Research Agency (STORE-EX Labex Project ANR-10-LABX-76-01) for financial support for their research on the electrochemical energy storage. The authors thank Cathy Denage, Laëtitia Etienne and Eric Lebraud at ICMCB for their technical support for ICP-OES, granulometry and XRD respectively. The authors thank Philippe Legros and Pascale Garreta at PLACAMAT and Marie-Anne Dourges at ISM for their scientific support with SEM, preparation of samples sections by cross polishing and BET analyses. The authors also thank Jérémy Humez at SAFT for its scientific support with electrochemical characterizations in Lithium-ion and all-solid-state batteries.

REFERENCES

(1) Stampatori, D.; Raimondi, P. P.; Noussan, M. Li-Ion Batteries: A Review of a Key Technology for Transport Decarbonization. *Energies* **2020**, *13* (10), 2638.

(2) Rozier, P.; Tarascon, J. M. Review - Li-Rich Layered Oxide Cathodes for Next-Generation Li-Ion Batteries: Chances and Challenges. *J. Electrochem. Soc.* **2015**, *162* (14), A2490-A2499.

(3) Manthiram, A.; Knight, J. C.; Myung, S.-T.; Oh, S.-M.; Sun, Y.-K. Nickel-Rich and Lithium-Rich Layered Oxide Cathodes: Progress and Perspectives. *Adv. Energy Mater.* **2016**, *6* (1), 1501010.

(4) Mohamed, N.; Allam, N. K. Recent Advances in the Design of Cathode Materials for Li-Ion Batteries. *RSC Adv.* **2020**, *10* (37), 21662-21685.

(5) Pu, K.-C.; Zhang, X.; Qu, X.-L.; Hu, J.-J.; Li, H.-W.; Gao, M.-X.; Pan, H.-G.; Liu, Y.-F. Recently Developed Strategies to Restrain Dendrite Growth of Li Metal Anodes for Rechargeable Batteries. *Rare Met.* **2020**, *39* (6), 616-635.

(6) Chen, J.; Wu, J.; Wang, X.; Zhou, A.; Yang, Z. Research Progress and Application Prospect of Solid-State Electrolytes in Commercial Lithium-Ion Power Batteries. *Energy Storage Mater.* **2021**, *35*, 70-87.

(7) Arya, A.; Sharma, A. L. A Glimpse on All-Solid-State Li-Ion Battery (ASSLIB) Performance Based on Novel Solid Polymer Electrolytes: A Topical Review. *J. Mater. Sci.* **2020**, *55* (15), 6242-6304.

(8) Placke, T.; Kloepsch, R.; Dühnen, S.; Winter, M. Lithium Ion, Lithium Metal, and Alternative Rechargeable Battery Technologies: The Odyssey for High Energy Density. *J Solid State Electrochem.* **2017**, *21* (7), 1939-1964.

(9) Wang, Q.; Ping, P.; Zhao, X.; Chu, G.; Sun, J.; Chen, C. Thermal Runaway Caused Fire and Explosion of Lithium Ion Battery. *J. Power Sources* **2012**, *208*, 210-224.

(10) Chombo, P. V.; Laoonual, Y. A Review of Safety Strategies of a Li-Ion Battery. *J. Power Sources* **2020**, *478*, 228649.

(11) Wang, D.; Zheng, L.; Li, X.; Du, G.; Feng, Y.; Jia, L.; Dai, Z. Effect of High Ni on Battery Thermal Safety. *Int. J. Energy Res.* **2020**, 1-11.

(12) Xie, H. J.; Sun, J.; Li, J. G.; Zhou, T.; Wei, S. P.; Yi, Z. H. Lithium-Ion Battery Thermal Runaway Electro-Thermal Triggering Method and Toxicity Analysis. *IOP Conf. Ser.: Earth Environ. Sci.* **2021**, *701*, 012007.

(13) Geng, L.; Liu, J.; Wood, D. L.; Qin, Y.; Lu, W.; Jafta, C. J.; Bai, Y.; Belharouak, I. Probing Thermal Stability of Li-Ion Battery Ni-Rich Layered Oxide Cathodes by Means of Operando Gas Analysis and Neutron Diffraction. *ACS Appl. Energy Mater.* **2020**, *3* (7), 7058-7065.

(14) Zheng, Y.; Xu, N.; Chen, S.; Liao, Y.; Zhong, G.; Zhang, Z.; Yang, Y. Construction of a Stable $LiNi_{0.8}Co_{0.1}Mn_{0.1}O_2$ (NCM811) Cathode Interface by a Multifunctional Organosilicon Electrolyte Additive. *ACS Appl. Energy Mater.* **2020**, *3* (3), 2837-2845.

(15) Seok, J.-W.; Lee, J.; Rodgers, T.; Ko, D.-H.; Shim, J.-H. Effect of $LiPO_2F_2$ Electrolyte Additive on Surface Electrical Properties of $LiNi_{0.6}Co_{0.2}Mn_{0.2}O_2$ Cathode. *Trans. Electr. Electron. Mater.* **2019**, *20* (6), 548-553.

(16) Khodr, Z.; Mallet, C.; Daigle, J.-C.; Feng, Z.; Amouzegar, K.; Claverie, J.; Zaghib, K. Electrochemical Study of Functional Additives for Li-Ion Batteries. *J. Electrochem. Soc.* **2020**, *167* (12), 120535.

(17) Zhang, Q.; Liu, S.; Lin, Z.; Wang, K.; Chen, M.; Xu, K.; Li, W. Highly Safe and Cyclable Li-Metal Batteries with Vinylethylene Carbonate Electrolyte. *Nano Energy* **2020**, *74*, 104860.

(18) Mwemezi, M.; Phiri, I.; Bon, C. Y.; Afrifah, V. A.; Kim, B. C.; Pyo, M.; Hamenu, L.; Madzvamuse, A.; Lee, K.; Ko, J. M.; Kim, Y. J. Hydroxyl Terminated Poly(Dimethylsiloxane) as an Electrolyte Additive to Enhance the Cycle Performance of Lithium-Ion Batteries. *Curr. Appl Phys.* **2020**.

(19) Deng, B.; Li, J.; Shang, H.; Liu, W.; Wan, Q.; Chen, M.; Qu, M.; Peng, G. Improving Cyclic Stability of $LiNi_{0.6}Co_{0.2}Mn_{0.2}O_2$-$SiO_x$/Graphite Full Cell Using Tris(Trimethylsilyl)Phosphite and Fluoroethylene Carbonate as Combinative Electrolyte Additive. *Ionics* **2020**.

(20) Wang, R.; Dai, X.; Qian, Z.; Sun, Y.; Fan, S.; Xiong, K.; Zhang, H.; Wu, F. In Situ Surface Protection for Enhancing Stability and Performance of $LiNi_{0.5}Mn_{0.3}Co_{0.2}O_2$ at 4.8V: The Working Mechanisms. *ACS Mater. Lett.* **2020**, *2* (4), 280-290.

(21) Wang, L.; Ma, J.; Wang, C.; Yu, X.; Liu, R.; Jiang, F.; Sun, X.; Du, A.; Zhou, X.; Cui, G. Novel Bifunctional Self-Stabilized Strategy Enabling 4.6 V $LiCoO_2$ with Excellent Long-Term Cyclability and High-Rate Capability *Adv. Sci.* **2019**, *6*, 1900355-1900365.

(22) Chen, C.; Jiang, M.; Zhou, T.; Raijmakers, L.; Vezhlev, E.; Wu, B.; Schülli, T. U.; Danilov, D. L.; Wei, Y.; Eichel, R.; Notten, P. H. L. Interface Aspects in All- Solid- State Li- Based Batteries Reviewed. *Adv. Energy Mater.* **2021**, *11* (13), 2003939.

(23) Banerjee, A.; Wang, X.; Fang, C.; Wu, E. A.; Meng, Y. S. Interfaces and Interphases in All-Solid-State Batteries with Inorganic Solid Electrolytes. *Chem. Rev.* **2020**, *120* (14), 6878-6933.

(24) Pang, Y.; Pan, J.; Yang, J.; Zheng, S.; Wang, C. Electrolyte/Electrode Interfaces in All-Solid-State Lithium Batteries: A Review. *Electrochem. Energy Rev.* **2021**, *4* (2), 169-193.

(25) Koerver, R.; Aygün, I.; Leichtweiß, T.; Dietrich, C.; Zhang, W.; Binder, J. O.; Hartmann, P.; Zeier, W. G.; Janek, J. Capacity Fade in Solid-State Batteries: Interphase Formation and Chemomechanical Processes in Nickel-Rich Layered Oxide Cathodes and Lithium Thiophosphate Solid Electrolytes. *Chem. Mater.* **2017**, *29* (13), 5574-5582.

(26) Wang, P.; Qu, W.; Song, W.; Chen, H.; Chen, R.; Fang, D. Electro-Chemo-Mechanical Issues at the Interfaces in Solid- State Lithium Metal Batteries. *Adv. Funct. Mater.* **2019**, 1900950.

(27) Strauss, F.; de Biasi, L.; Kim, A.-Y.; Hertle, J.; Schweidler, S.; Janek, J.; Hartmann, P.; Brezesinski, T. Rational Design of Quasi-Zero-Strain NCM Cathode Materials for Minimizing Volume Change Effects in All-Solid-State Batteries. *ACS Mater. Lett.* **2020**, *2* (1), 84-88.

(28) Conforto, G.; Ruess, R.; Schröder, D.; Trevisanello, E.; Fantin, R.; Richter, F. H.; Janek, J. Editors' Choice—Quantification of the Impact of Chemo-Mechanical Degradation on the Performance and Cycling Stability of NCM-Based Cathodes in Solid-State Li-Ion Batteries. *J. Electrochem. Soc.* **2021**, *168* (7), 070546.

(29) Koerver, R.; Zhang, W.; de Biasi, L.; Schweidler, S.; Kondrakov, A. O.; Kolling, S.; Brezesinski, T.; Hartmann, P.; Zeier, W. G.; Janek, J. Chemo-Mechanical Expansion of Lithium Electrode Materials – on the Route to Mechanically Optimized All-Solid-State Batteries. *Energy Environ. Sci.* **2018**, *11* (8), 2142-2158.

(30) Ren, Y.; Shen, Y.; Lin, Y.; Nan, C.-W. Direct Observation of Lithium Dendrites inside Garnet-Type Lithium-Ion Solid Electrolyte. *Electrochem. Commun.* **2015**, *57*, 27-30.

(31) Han, F.; Westover, A. S.; Yue, J.; Fan, X.; Wang, F.; Chi, M.; Leonard, D. N.; Dudney, N. J.; Wang, H.; Wang, C. High Electronic Conductivity as the Origin of Lithium Dendrite Formation within Solid Electrolytes. *Nat. Energy* **2019**, *4* (3), 187-196.

(32) Porz, L.; Swamy, T.; Sheldon, B. W.; Rettenwander, D.; Frömling, T.; Thaman, H. L.; Berendts, S.; Uecker, R.; Carter, W. C.; Chiang, Y.-M. Mechanism of Lithium Metal Penetration through Inorganic Solid Electrolytes. *Adv. Energy Mater.* **2017**, *7*, 1701003.

(33) Liang, L.; Du, K.; Peng, Z.; Cao, Y.; Duan, J.; Jiang, J.; Hu, G. Co-Precipitation Synthesis of $Ni_{0.6}Co_{0.2}Mn_{0.2}(OH)_2$ Precursor and Characterization of $LiNi_{0.6}Co_{0.2}Mn_{0.2}O_2$ Cathode Material for Secondary Lithium Batteries. *Electrochim. Acta* **2014**, *130*, 82–89.

(34) Zybert, M.; Ronduda, H.; Szczęsna, A.; Trzeciak, T.; Ostrowski, A.; Żero, E.; Wieczorek, W.; Raróg-Pilecka, W.; Marcinek, M. Different Strategies of Introduction of Lithium Ions into

Nickel‐ manganese‐ cobalt Carbonate Resulting in $LiNi_{0.6}Mn_{0.2}Co_{0.2}O_2$ (NMC622) Cathode Material for Li-Ion Batteries. *Solid State Ionics* **2020**, *348*, 115273.

(35) Ma, Y.; Li, L.; Wang, L.; Luo, R.; Xu, S.; Wu, F.; Chen, R. Effect of Metal Ion Concentration in Precursor Solution on Structure and Electrochemical Performance of $LiNi_{0.6}Co_{0.2}Mn_{0.2}O_2$. *J. Alloys Compd.* **2019**, *778*, 643-651.

(36) Li, F.; Liu, Z.; Shen, J.; Xu, X.; Zeng, L.; Li, Y.; Zhang, D.; Zuo, S.; Liu, J. Ni-Rich Layered Oxide with Preferred Orientation (110) Plane as a Stable Cathode Material for High-Energy Lithium-Ion Batteries. *Nanomaterials* **2020**, *10* (12), 2495.

(37) Ronduda, H.; Zybert, M.; Szczęsna-Chrzan, A.; Trzeciak, T.; Ostrowski, A.; Szymański, D.; Wieczorek, W.; Raróg-Pilecka, W.; Marcinek, M. On the Sensitivity of the Ni-Rich Layered Cathode Materials for Li-Ion Batteries to the Different Calcination Conditions. *Nanomaterials* **2020**, *10* (10), 2018.

(38) Wang, L.; Wu, B.; Mu, D.; Liu, X.; Peng, Y.; Xu, H.; Liu, Q.; Gai, L.; Wu, F. Single-Crystal $LiNi_{0.6}Co_{0.2}Mn_{0.2}O_2$ as High Performance Cathode Materials for Li-Ion Batteries. *J. Alloys Compd.* **2016**, *674*, 360-367.

(39) Xia, Y.-F.; Nie, M.; Wang, Z.-B.; Yu, F.-D.; Zhang, Y.; Zheng, L.-L.; Wu, J.; Ke, K. Structural, Morphological and Electrochemical Investigation of $LiNi_{0.6}Co_{0.2}Mn_{0.2}O_2$ Cathode Material Synthesized in Different Sintering Conditions. *Ceram. Int.* **2015**, *41* (9), 11815-11823.

(40) Li, H.; Li, J.; Ma, X.; Dahn, J. R. Synthesis of Single Crystal $LiNi_{0.6}Mn_{0.2}Co_{0.2}O_2$ with Enhanced Electrochemical Performance for Lithium Ion Batteries. *J. Electrochem. Soc.* **2018**, *165* (5), A1038-A1045.

(41) Noh, H.-J.; Youn, S.; Yoon, C. S.; Sun, Y.-K. Comparison of the Structural and Electrochemical Properties of Layered $Li[Ni_xCo_yMn_z]O_2$ (x = 1/3, 0.5, 0.6, 0.7, 0.8 and 0.85) Cathode Material for Lithium-Ion Batteries. *J. Power Sources* **2013**, *233*, 121-130.

(42) Soloy, A.; Flahaut, D.; Allouche, J.; Foix, D.; Salvato Vallverdu, G.; Suard, E.; Dumont, E.; Gal, L.; Weill, F.; Croguennec, L. Effect of Particle Size on $LiNi_{0.6}Mn_{0.2}Co_{0.2}O_2$ Layered Oxide Performance in Li-Ion Batteries. *ACS Appl. Energy Mater.* (DOI: 0.1021/acsaem.1c03924)

(43) Rodriguez-Carvajal, J. Recent Advances in Magnetic Structure Determination by Neutron Powder Diffraction. *Physica B.* **1993**, *192*, 55-69.

(44) Scofield, J. H. Hartree-Slater Subshell Photoionization Cross-Sections at 1254 and 1487 eV. *J. Electron. Spectrosc. Relat. Phenom.* **1976**, *8*, 129-137.

(45) Liu, M.; Wang, Y.; Li, M.; Li, G.; Li, B.; Zhang, S.; Ming, H.; Qiu, J.; Chen, J.; Zhao, P. A New Composite Gel Polymer Electrolyte Based on Matrix of PEGDA with High Ionic Conductivity for Lithium-Ion Batteries. Electrochim. Acta 2020, 354, 136622.

(46) Yin, S.-C.; Rho, Y.-H.; Swainson, I.; Nazar, L. F. X-Ray/Neutron Diffraction and Electrochemical Studies of Lithium De/Re-Intercalation in $Li_{1-x}Co_{1/3}Ni_{1/3}Mn_{1/3}O_2$ (x=0→1). *Chem. Mater.* **2006**, *18* (7), 1901-1910.

(47) Hartmann, L.; Pritzl, D.; Beyer, H.; Gasteiger, H. A. Evidence for Li^+/H^+ Exchange during Ambient Storage of Ni-Rich Cathode Active Materials. *J. Electrochem. Soc.* **2021**, *168* (7), 070507.

(48) Martinez, A. C.; Grugeon, S.; Cailleu, D.; Courty, M.; Tran-Van, P.; Delobel, B.; Laruelle, S. High Reactivity of the Nickel-Rich $LiNi_{1-x-y}Mn_xCo_yO_2$ Layered Materials Surface towards H_2O/CO_2 Atmosphere and $LiPF_6$-Based Electrolyte. *J. Power Sources* **2020**, *468*, 228204.

(49) Busà, C.; Belekoukia, M.; Loveridge, M. J. The Effects of Ambient Storage Conditions on the Structural and Electrochemical Properties of NMC-811 Cathodes for Li-Ion Batteries. *Electrochim. Acta* **2021**, *366*, 137358.

(50) Dedryvère, R.; Gireaud, L.; Grugeon, S.; Laruelle, S.; Tarascon, J.-M.; Gonbeau, D. Characterization of Lithium Alkyl Carbonates by X-Ray Photoelectron Spectroscopy: Experimental and Theoretical Study. *J. Phys. Chem. B* **2005**, *109* (33), 15868-15875.

(51) Dedryvère, R.; Foix, D.; Franger, S.; Patoux, S.; Daniel, L.; Gonbeau, D. Electrode/Electrolyte Interface Reactivity in High-Voltage Spinel $LiMn_{1.6}Ni_{0.4}O_4/Li_4Ti_5O_{12}$ Lithium-Ion Battery. *J. Phys. Chem. C* **2010**, *114* (24), 10999-11008.

(52) Dahéron, L.; Dedryvère, R.; Martinez, H.; Ménétrier, M.; Denage, C.; Delmas, C.; Gonbeau, D. Electron Transfer Mechanisms upon Lithium Deintercalation from $LiCoO_2$ to CoO_2 Investigated by XPS. *Chem. Mater.* **2008**, *20* (2), 583-590.

(53) Zhang, Y.; Du, K.; Cao, Y.; Lu, Y.; Peng, Z.; Fan, J.; Li, L.; Xue, Z.; Su, H.; Hu, G. Hydrothermal Preparing Agglomerate LiNi0.8Co0.1Mn0.1O2 Cathode Material with Submicron Primary Particle for Alleviating Microcracks. *Journal of Power Sources* **2020**, *477*, 228701. https://doi.org/10.1016/j.jpowsour.2020.228701.

(54) Wei, W.; Ding, Z.; Chen, C.; Yang, C.; Han, B.; Xiao, L.; Liang, C.; Gao, P.; Cho, K. Surface-Dependent Stress-Corrosion Cracking in Ni-Rich Layered Oxide Cathodes. *Acta Materialia* **2021**, *212*, 116914. https://doi.org/10.1016/j.actamat.2021.116914.

(55) Ryu, H.-H.; Park, K.-J.; Yoon, C. S.; Sun, Y.-K. Capacity Fading of Ni-Rich Li[NixCoyMn1– x – y]O 2 ($0.6 \leq x \leq 0.95$) Cathodes for High-Energy-Density Lithium-Ion Batteries: Bulk or Surface Degradation? Chem. Mater. 2018, 30 (3), 1155–1163. https://doi.org/10.1021/acs.chemmater.7b05269.

(56) Bi, Y.; Tao, J.; Wu, Y.; Li, L.; Xu, Y.; Hu, E.; Wu, B.; Hu, J.; Wang, C.; Zhang, J.-G.; Qi, Y.; Xiao, J. Reversible Planar Gliding and Microcracking in a Single-Crystalline Ni-Rich Cathode. *Science* **2020**, *370* (6522), 1313–1317. https://doi.org/10.1126/science.abc3167.

(57) Dedryvère, R.; Foix, D.; Franger, S.; Patoux, S.; Daniel, L.; Gonbeau, D. Electrode/Electrolyte Interface Reactivity in High-Voltage Spinel $LiMn_{1.6}Ni_{0.4}O_4/Li_4Ti_5O_{12}$ Lithium-Ion Battery. *J. Phys. Chem. C* **2010**, *114* (24), 10999–11008. https://doi.org/10.1021/jp1026509.

(58) Kim, H.; Kim, M. G.; Jeong, H. Y.; Nam, H.; Cho, J. A New Coating Method for Alleviating Surface Degradation of $LiNi_{0.6}Co_{0.2}Mn_{0.2}O_2$ Cathode Material: Nanoscale Surface Treatment of Primary Particles. *Nano Lett.* **2015**, *15* (3), 2111–2119. https://doi.org/10.1021/acs.nanolett.5b00045.

(59) Ruess, R.; Schweidler, S.; Hemmelmann, H.; Conforto, G.; Bielefeld, A.; Weber, D. A.; Sann, J.; Elm, M. T.; Janek, J. Influence of NCM Particle Cracking on Kinetics of Lithium-Ion Batteries with Liquid or Solid Electrolyte. *J. Electrochem. Soc.* **2020**, *167* (10), 100532.

(60) Gauthier, N.; Courrèges, C.; Demeaux, J.; Tessier, C.; Martinez, H. Influence of the Cathode Potential on Electrode Interactions within a $Li_4Ti_5O_{12}$ vs $LiNi_{3/5}Mn_{1/5}Co_{1/5}O_2$ Li-Ion Battery. *J. Electrochem. Soc.* **2020**, *167* (4), 040504.

(61) Karayaylali, P.; Zhang, Y.; Giordano, L.; Katayama, Y.; Tatara, R.; Yu, Y.; Maglia, F.; Jung, R.; Shao-Horn, Y. The Role of Diphenyl Carbonate Additive on the Interfacial Reactivity of Positive Electrodes in Li-Ion Batteries. *J. Electrochem. Soc.* **2020**, *167* (4), 040522.

(62) Yu, X.; Manthiram, A. A Long Cycle Life, All-Solid-State Lithium Battery with a Ceramic-Polymer Composite Electrolyte. *ACS Appl. Energy Mater.* **2020**, *3* (3), 2916-2924.

(63) Yang, H.; Bright, J.; Chen, B.; Zheng, P.; Gao, X.; Liu, B.; Kasani, S.; Zhang, X.; Wu, N. Chemical Interaction and Enhanced Interfacial Ion Transport in a Ceramic Nanofiber-Polymer Composite Electrolyte for All-Solid-State Lithium Metal Batteries. *J. Mater. Chem. A* **2020**, *8* (15), 7261-7272.

(64) Nkosi, F. P.; Valvo, M.; Mindemark, J.; Dzulkurnain, N. A.; Hernández, G.; Mahun, A.; Abbrent, S.; Brus, J.; Kobera, L.; Edström, K. Garnet-Poly(ε-Caprolactone- *Co* -Trimethylene Carbonate) Polymer-in-Ceramic Composite Electrolyte for All-Solid-State Lithium-Ion Batteries. *ACS Appl. Energy Mater.* **2021**, *4* (3), 2531-2542.

(65) López-Aranguren, P.; Judez, X.; Chakir, M.; Armand, M.; Buannic, L. High Voltage Solid State Batteries: Targeting High Energy Density with Polymer Composite Electrolytes. *J. Electrochem. Soc.* **2020**, *167* (2), 020548.

(66) Han, B.; Jiang, P.; Li, S.; Lu, X. Functionalized Gel Polymer Electrolyte Membrane for High Performance Li Metal Batteries. *Solid State Ionics* **2021**, *361*, 115572.

(67) Li, H.; Liu, W.; Yang, X.; Xiao, J.; Li, Y.; Sun, L.; Ren, X.; Zhang, P.; Mi, H. Fluoroethylene Carbonate-Li-Ion Enabling Composite Solid-State Electrolyte and Lithium Metal Interface Self-Healing for Dendrite-Free Lithium Deposition. *Chem. Eng. J.* **2021**, *408*, 127254.

(68) Zhang, X.; Liu, T.; Zhang, S.; Huang, X.; Xu, B.; Lin, Y.; Xu, B.; Li, L.; Nan, C.-W.; Shen, Y. Synergistic Coupling between $Li_{6.75}La_3Zr_{1.75}Ta_{0.25}O_{12}$ and Poly(Vinylidene Fluoride) Induces High Ionic Conductivity, Mechanical Strength, and Thermal Stability of Solid Composite Electrolytes. *J. Am. Chem. Soc.* **2017**, *139* (39), 13779-13785.

(69) Martinez, A. I. P.; Aguesse, F.; Otaegui, L.; Schneider, M.; Roters, A.; Llordés, A.; Buannic, L. The Cathode Composition, A Key Player in the Success of Li-Metal Solid-State Batteries. *J. Phys. Chem. C* **2019**, *123*, 3270-3278.

(70) Xu, D.; Su, J.; Jin, J.; Sun, C.; Ruan, Y.; Chen, C.; Wen, Z. In Situ Generated Fireproof Gel Polymer Electrolyte with $Li_{6.4}Ga_{0.2}La_3Zr_2O_{12}$ As Initiator and Ion- Conductive Filler. *Adv. Energy Mater.* **2019**, *9* (25), 1900611.

(71) Monroe, C.; Newman, J. The Impact of Elastic Deformation on Deposition Kinetics at Lithium/Polymer Interfaces. *J. Electrochem. Soc.* **2005**, *152* (2), A396-A404.

(72) Xu, R.; Cheng, X.-B.; Yan, C.; Zhang, X.-Q.; Xiao, Y.; Zhao, C.-Z.; Huang, J.-Q.; Zhang, Q.; Artificial Interphases for Highly Stable Lithium Metal Anode. *Matter* **2019**, *1*, 317-344.

(73) Han, X.; Gong, Y.; Fu, K. (Kelvin); He, X.; Hitz, G. T.; Dai, J.; Pearse, A.; Liu, B.; Wang, H.; Rubloff, G.; Mo, Y.; Thangadurai, V.; Wachsman, E. D.; Hu, L. Negating Interfacial Impedance in Garnet-Based Solid-State Li Metal Batteries. *Nat. Mater.* **2017**, *16* (5), 572-579.

(74) Fu, K. (Kelvin); Gong, Y.; Liu, B.; Zhu, Y.; Xu, S.; Yao, Y.; Luo, W.; Wang, C.; Lacey, S. D.; Dai, J.; Chen, Y.; Mo, Y.; Wachsman, E.; Hu, L. Toward Garnet Electrolyte-Based Li Metal Batteries: An Ultrathin, Highly Effective, Artificial Solid-State Electrolyte/Metallic Li Interface. *Sci. Adv.* **2017**, *3* (4), e1601659.

(75) Luo, W.; Gong, Y.; Zhu, Y.; Fu, K. K.; Dai, J.; Lacey, S. D.; Wang, C.; Liu, B.; Han, X.; Mo, Y.; Wachsman, E. D.; Hu, L. Transition from Superlithiophobicity to Superlithiophilicity of Garnet Solid-State Electrolyte. *J. Am. Chem. Soc.* **2016**, *138* (37), 12258-12262.

(76) Luo, W.; Gong, Y.; Zhu, Y.; Li, Y.; Yao, Y.; Zhang, Y.; Fu, K. (Kelvin); Pastel, G.; Lin, C.; Mo, Y.; Wachsman, E. D.; Hu, L. Reducing Interfacial Resistance between Garnet- Structured Solid- State Electrolyte and Li- Metal Anode by a Germanium Layer. *Adv. Mater.* **2017**, *29* (22), 1606042.

(77) Liu, Y.; Li, C.; Li, B.; Song, H.; Cheng, Z.; Chen, M.; He, P.; Zhou, H. Germanium Thin Film Protected Lithium Aluminum Germanium Phosphate for Solid-State Li Batteries. *Adv. Energy Mater.* **2018**, *8* (16), 1702374.

(78) Wang, C.; Xie, H.; Zhang, L.; Gong, Y.; Pastel, G.; Dai, J.; Liu, B.; Wachsman, E. D.; Hu, L. Universal Soldering of Lithium and Sodium Alloys on Various Substrates for Batteries. *Adv. Energy Mater.* **2018**, *8* (6), 1701963.

(79) He, M.; Cui, Z.; Chen, C.; Li, Y.; Guo, X. Formation of Self-Limited, Stable and Conductive Interfaces between Garnet Electrolytes and Lithium Anodes for Reversible Lithium Cycling in Solid-State Batteries. *J. Mater. Chem. A* **2018**, *6* (24), 11463-11470.

(80) Lu, Y.; Huang, X.; Song, Z.; Rui, K.; Wang, Q.; Gu, S.; Yang, J.; Xiu, T.; Badding, M. E.; Wen, Z. Highly Stable Garnet Solid Electrolyte Based Li-S Battery with Modified Anodic and Cathodic Interfaces. *Energy Storage Mater.* **2018**, *15*, 282-290.

(81) Zhou, W.; Wang, S.; Li, Y.; Xin, S.; Manthiram, A.; Goodenough, J. B. Plating a Dendrite-Free Lithium Anode with a Polymer/Ceramic/Polymer Sandwich Electrolyte. *J. Am. Chem. Soc.* **2016**, *138* (30), 9385-9388.

(82) Wang, C.; Yang, Y.; Liu, X.; Zhong, H.; Xu, H.; Xu, Z.; Shao, H.; Ding, F. Suppression of Lithium Dendrite Formation by Using LAGP-PEO (LiTFSI) Composite Solid Electrolyte and Lithium Metal Anode Modified by PEO (LiTFSI) in All-Solid-State Lithium Batteries. *ACS Appl. Mater. Interfaces* **2017**, *9* (15), 13694-13702.

(83) Bae, J.; Qian, Y.; Li, Y.; Zhou, X.; Goodenough, J. B.; Yu, G. Polar Polymer-Solvent Interaction Derived Favorable Interphase for Stable Lithium Metal Batteries. *Energy Environ. Sci.* **2019**, *12* (11), 3319-3327.

(84) Duan, H.; Fan, M.; Chen, W.-P.; Li, J.-Y.; Wang, P.-F.; Wang, W.-P.; Shi, J.-L.; Yin, Y.-X.; Wan, L.-J.; Guo, Y.-G. Extended Electrochemical Window of Solid Electrolytes via Heterogeneous Multilayered Structure for High- Voltage Lithium Metal Batteries. *Adv. Mater.* **2019**, *31*, 1807789.

(85) Wang, C.; Bai, G.; Yang, Y.; Liu, X.; Shao, H. Dendrite-Free All-Solid-State Lithium Batteries with Lithium Phosphorous Oxynitride-Modified Lithium Metal Anode and Composite Solid Electrolytes. *Nano Res.* **2019**, *12*, 217-223.

(86) Sheng, O., Zheng, J., Ju, Z., Jin, C., Wang, Y., Chen, M., Nai, J., Liu, T., Zhang, W., Liu, Y., Tao, X., In Situ Construction of a LiF-Enriched Interface for Stable All-Solid-State Batteries and its Origin Revealed by Cryo-TEM. *Adv. Mater.* **2020**, *32*, 2000223.

(87) Liu, Y.; Tao, X.; Wang, Y.; Jiang, C.; Ma, C.; Sheng, O.; Lu, G.; Lou, X.W.D. Self-assembled monolayers direct a LiF-rich interphase toward long-life lithium metal batteries. *Science* **2022**, *375*(6582), 739-745.

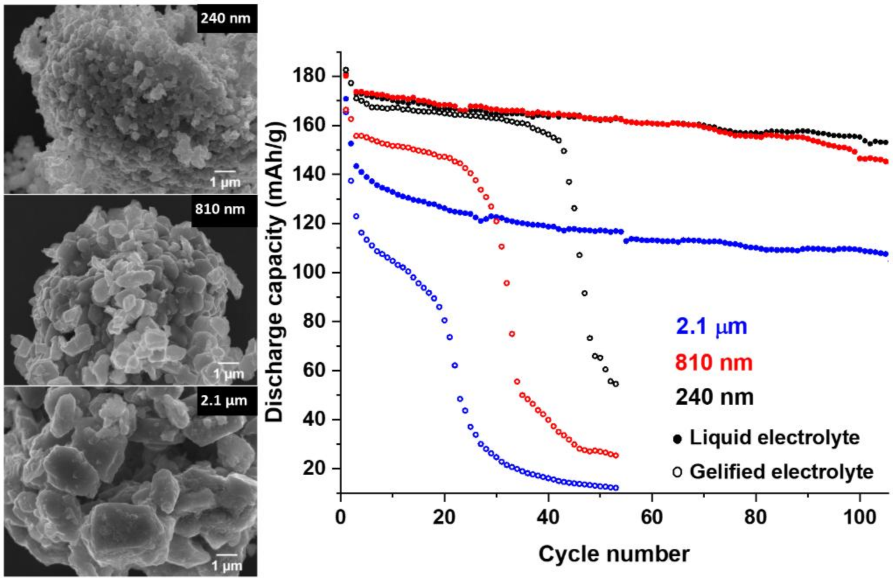

For Table of contents only